Electron heating associated with magnetic reconnection in foreshock waves: particle-in-cell simulation analysis

Shan Wang[1] and Yan Yang[2]

[1]Peking University
[2]University of Delaware

May 25, 2023

Abstract

Magnetic reconnection occurs in turbulent plasmas like shock transition regions, while its exact role in energy dissipation therein is not yet clear. We perform a 2D particle-in-cell simulation for foreshock waves and study electron heating associated with reconnection. The probability distribution of Te exhibits a shift to higher values near reconnection X-lines compared to elsewhere. By examining the Te evolution using the superposed epoch analysis, we find that Te is higher in reconnection than in non-reconnecting current sheets, and Te increases over the ion cyclotron time scale. The heating rate of Te is 10%-40% miVA2, where VA is the average ion Alfvén speed in reconnection regions, which demonstrates the importance of reconnection in heating electrons. We further investigate the bulk electron energization mechanisms by decomposing under guiding center approximations. Around the reconnection onset, E|| dominates the total energization partly contributed by electron holes, and the perpendicular energization is dominant by the magnetization term associated with the gyro-motion in the inhomogeneous fields. The Fermi mechanism contributes negative energization at early time mainly due to the Hall effect, and later the outflow in the reconnection plane contributes more dominant positive values. After a couple of ion cyclotron periods from reconnection onset, the Fermi mechanism dominates the energization. A critical factor for initiating reconnection is to drive current sheets to the de-scale thickness. The reconnection structures can be complicated due to flows originated from the ion-scale waves, and interactions between multiple reconnection sites. These features may assist future analysis of observation data.

Electron heating associated with magnetic reconnection in foreshock waves: particle-in-cell simulation analysis

Shan Wang[1*], and Yan Yang[2]

[1]Institute of Space Physics and Applied Technology, Peking University, Beijing 100871, China

[2]Department of Physics and Astronomy, University of Delaware, Newark, DE 19716, USA

*coralwang90@gmail.com

Key points

- Statistically electrons are heated in reconnection with the temperature increase at 10%~40% of the available magnetic energy for reconnection
- The electron bulk energization is dominant by $E_{\parallel}$ around reconnection onset, and is later dominant by Fermi acceleration
- Driving the current sheet to the d_e-scale thickness is critical for initiating reconnection, and interactions of multiple reconnection sites lead to complicated structures

Abstract

Magnetic reconnection occurs in turbulent plasmas like shock transition regions, while its exact role in energy dissipation therein is not yet clear. We perform a 2D particle-in-cell simulation for foreshock waves and study electron heating associated with reconnection. The probability distribution of T_e exhibits a shift to higher values near reconnection X-lines compared to elsewhere. By examining the T_e evolution using the superposed epoch analysis, we find that T_e is higher in reconnection than in non-reconnecting current sheets, and T_e increases over the ion cyclotron time scale. The heating rate of T_e is 10%-40% $m_i V_A^2$, where V_A is the average ion Alfvén speed in reconnection regions, which demonstrates the importance of reconnection in heating electrons. We further investigate the bulk electron energization mechanisms by decomposing $\boldsymbol{j_e} \cdot \boldsymbol{E}$ under guiding center approximations. Around the reconnection onset, $E_{||}$ dominates the total energization partly contributed by electron holes, and the perpendicular energization is dominant by the magnetization term associated with the gyro-motion in the inhomogeneous fields. The Fermi mechanism contributes negative energization at early time mainly due to the Hall effect, and later the outflow in the reconnection plane contributes more dominant positive values. After a couple of ion cyclotron periods from reconnection onset, the Fermi mechanism dominates the energization. A critical factor for initiating reconnection is to drive current sheets to the d_e-scale thickness. The reconnection structures can be complicated due to flows originated from the ion-scale waves, and interactions between multiple reconnection sites. These features may assist future analysis of observation data.

1. Introduction

Magnetic reconnection is a ubiquitous plasma process that converts energies from electromagnetic fields to particles. Commonly happening in the turbulent environment, such as the Earth's magnetosheath [e.g., Voros et al., 2017; Phan et al., 2018; Starwarz et al., 2022; Wilder et al., 2022] and the shock transition region [e.g., Gingell et al., 2019, 2020; Wang et al., 2019, 2020; Liu et al., 2020], reconnection can potentially contribute to the energy dissipation therein. In observations, the clearest reconnection signature is the outflow jet for electrons [e.g., Phan et al., 2018], sometimes for ions [e.g., Wang et al., 2019], and the inflow and outflow of the magnetic flux [e.g., Qi et al., 2022]. The outflow is also the primary criterion for identifying reconnection events. The effect on electron heating is less clear. Some individual events exhibit T_e enhancements in the reconnection current sheets [e.g., Gingell et al., 2019; Wang et al., 2019; Liu et al., 2020], and some do not [e.g., Phan et al., 2018; Wang et al., 2020]. A statistical examination [Gingell et al., 2020] shows that the electron heating rate ($\Delta T_e/m_i V_A^2$, i.e., the temperature increase from inflow to outflow regions of reconnection with respect to the inflow magnetic energy) can be either positive or negative. The width of the heating rate distribution is much greater than that in typical magnetopause reconnection of 1.7% [Phan et al., 2013], and can exceed 100% in some cases. As discussed in Gingell et al. [2020], electron heating may also occur outside of the reconnection current sheets in the shock transition region, which complicates the observation features. Recent simulation studies have shown that reconnection in turbulence contributes to electron heating: Shay et al. [2018] found that the scaling of ion and electron heating in single reconnection events is applicable to turbulence, while the number of reconnecting X-lines is important in determining the actual heating amount; Bandyopadhyay et al. [2021] demonstrated electron heating in individual reconnection X-line regions diagnosed with the pressure work. Here we use a simulation to study electron heating in reconnection in the shock transition region, aiming to find out explicitly whether reconnection is important for heating electrons in such an environment, to understand the electron energization mechanisms in the framework of guiding center motion, and to advance the understanding of structures and evolution of reconnection in the shock turbulence.

For reconnection in the shock transition region, one pathway of generating reconnection current sheets is through the evolution of foreshock waves, as demonstrated by particle-in-cell (PIC) simulations [Bessho et al., 2020] and inferred from observations [Wang et al., 2020]. In the transition region of quasi-parallel shocks, the presence of counter-streaming ions between the incoming solar wind and the backstreaming population can initiate ion-ion beam instability and generate ULF waves with a wavelength of a few to tens of ion inertia lengths (d_i) [e.g., Eastwood et al., 2005; Wilson III, 2016]. The ULF wave grows into large amplitudes, sometimes generating non-linear structures like Short Large-Amplitude Magnetic Structures (SLAMS) [e.g., Schwartz et al., 1992; Wang et al., 2020; Chen et al., 2021]. The waveform in the ion-scale waves gradually distorts, and secondary instabilities may also be excited, which both lead to thin current sheets that eventually reconnect [Bessho et al., 2020]. In this study, we extract the foreshock environment in the shock to simulate the ion-ion instability and the processes that follow.

2. Simulation

We perform a 2D PIC simulation in the x-y plane using the VPIC code [Bowers, 2008]. The simulation starts from a homogeneous magnetic field $\mathbf{B}_0$ along x. A solar wind ion population moves with a bulk $V_x<0$, a backstreaming ion population moves with $V_x>0$, and electrons are at rest. The density ratio between backstreaming ions and electrons is $n_b/n_0=0.2$, the relative drift between two ion populations is $dV=15\ V_{A0}$, where V_{A0} is the ion Alfvén speed based on B_0 and n_0. The solar wind ion β is 1.0, the temperature ratio between backstreaming ions and solar wind ions is $T_b/T_{SW}=25$, and the temperature ratio between electrons and solar wind ions is $T_e/T_{SW}=2$. The simulation uses periodic boundary conditions along both directions. The system size is $L_x \times L_y=240\ d_i \times 120\ d_i$, the grid size in each dimension is 0.19 d_e, the mass ratio is $m_i/m_e=100$, and the electron plasma to cyclotron frequency ratio is $\omega_{pe}/\omega_{ce} = 5$. Unless otherwise noted, the magnetic and electric field are in units of B_0, density is in n_0, velocity is in speed of light (c), and temperature is in m_ec^2.

Under the simulated initial conditions, where n_b/n_0 and dV are the most critical parameters, the linear instability analysis predicts the excitation of the non-resonant mode ion-ion beam instability [e.g., Akimoto et al., 1993] (not shown). The corresponding ULF wave propagates toward -x with a right-hand polarization. The wave does not resonate with backstreaming ions (the reason for the name of 'non-resonant' mode) but cyclotron resonates with solar wind ions. Such simulation setups for 1D runs in the same parameter regime have been used to successfully produce the non-resonant ULF wave and the associated nonlinear solitary structures [Chen et al., 2021; Chen et al., 2022]. Here the simulation is extended to 2D, and it still leads to the non-resonant mode wave in the linear stage as predicted. The simulation represents the foreshock wave environment, and we will investigate its evolution, particularly about electron heating in reconnection born out of the foreshock waves.

3. Electron heating in reconnection current sheets

The simulation develops the non-resonant mode ion-ion instability. The corresponding wave has a wavelength of 6.7 d_i, propagating toward -x with a speed of 2.2 V_{A0} with a right-hand polarization, and the frequency is $\omega = 2.0\omega_{ci}$. At $t\omega_{ci} = 17.0$, the wave magnetic field $dB = \sqrt{B_y^2 + B_z^2}$ grows to the largest spatially averaged value of 2.2 B_0, with a local maximum amplitude of 7.3 B_0. The B_y field is shown in Figure 1a. The B_y stripes are mainly along y and have been broken into segments of current sheets. The overplotted magnetic field lines in the x-y plane (black curves) show the formation of islands that indicate reconnection, and the 'x' symbols mark the X-point locations determined by the saddle points of the vector potential A_z with optimal data smoothing [Haggerty et al., 2017]. T_e exhibits enhancements that tend to be associated with current sheets (Figure 1b).

We examined the evolution of individual reconnection current sheets. An example is shown in Figure 2 (a-e). Around $t\omega_{ci} = 16.0$, magnetic fields in the shown region of a few d_i are compressed to a strength of ~5 B_0 (Figure 2a), which can be considered as a SLAMS. The compressed region is associated with electron heating (Figure 2b). The current sheet in the center is further compressed to the electron scale and reconnection occurs at $t\omega_{ci} = 16.5$ (Figure 2c), where T_e is more significantly enhanced. The current sheet thickness when X-line first appears at $t\omega_{ci} = 16.5$ is 1.6 d_e, based on the full width at half maximum of j_M along N across the X-line (not shown). The LMN coordinate system is determined and illustrated on V_{eL} profiles (Figures 2d-2e): M=z is along the out-of-plane current direction; L is along the maximum variance direction of the x-y plane magnetic fields in a region of 2 d_i×2 d_i surrounding the X-line, and N finishes the right-handed L-M-N coordinate. V_{eL} exhibits a field-aligned shear flow on two sides of the current sheets. The flow shear develops before reconnection starts. It is originally the flow along the ion-scale wave magnetic fields as the wave grows to large amplitudes, and becomes the shear flow as field lines bend to form the current sheet. The shear flow gradually evolves into part of the reconnection outflow jet (Figure 2e). At $t\omega_{ci} = 16.5$, the shear flow is 6.3 $V_{A,asym}$, where $V_{A,asym} = \sqrt{\frac{|B_{L1}B_{L2}|(|B_{L1}|+|B_{L2}|)}{m_i(n_1|B_{L2}|+n_2|B_{L1}|)}}$ is the inflow ion Alfvén speed for asymmetric reconnection, and parameters for calculating the shear flow and $V_{A,asym}$ are taken at inflow regions where $|j_M|$ drops to 1/10 of its maximum. Ions are demagnetized and V_{iL} also exhibits diverging outflows but with a much smaller amplitude than V_{eL} (not shown), indicating that ions are involved in reconnection, but the region is not large enough to fully develop magnetized ion outflow jets. The shear flow is much greater than the critical value of ~2$V_{A,asym}$ (for weak asymmetry as in this current sheet) that was predicted to suppress reconnection [Doss et al., 2015]. We suspect that the incomplete coupling of ions may play a role in allowing for reconnection to happen, since the electron mass or something between ion and electron masses may be more appropriate to characterize the Alfvén speed that sets the shear flow threshold; the strong driving condition in the turbulence may also be helpful for sustaining reconnection. It requires future work to better understand whether and how shear flow effects on reconnection vary under these circumstances.

The turbulent environment generates many reconnection current sheets, and some can be close to and affected by each other. Figure 2f shows an example cluster of current sheets with multiple X-lines. Arrows indicate the inflow and outflow directions at each reconnection site, based on the consistent indicators of the direction of E_z, evolution of the A_z contours, and the direction of electron outflow jets. The islands generated by X-lines No. 1 and No. 2 connect to the inflow region of X-line No. 3, so the reconnection jets around these islands can help drive the inflow of reconnection No. 3. X-line No. 4 is in the exhaust of reconnection No. 3. A band of T_e enhancement spans from X-line No. 3 to the inflow region of reconnection No. 4, indicating the flow of energized particles between reconnection sites, and these particles can thus be energized by multiple reconnection sites. The source of energized particles from reconnection No. 3 also leads to a complicated T_e profile. Along the trajectory marked by the magenta line in Figure 2f, the enhanced T_e band from the different X-line leads to asymmetric inflow T_e conditions for reconnection site No. 4, and T_e in the exhaust is lower than T_e in the inflow. Such an observation feature might be mis-interpreted as low/negative heating rate by reconnection, but the high inflow T_e is actually due to other mechanisms rather than the observed reconnection current sheet.

The importance of reconnection in the statistical sense is evaluated by plotting the probability distribution function (pdf) of T_e (Figure 3). The plot is for $t\omega_{ci} = 18.0$, where the number of X-lines reaches the maximum of 328, while the features are persistent for all time steps with X-lines. Compared to the pdf of all cells (black), the pdf of T_e for cells at 2 $d_e \times 2$ d_e surrounding X-lines (red) is clearly shifted to higher T_e values. The pdf of T_e surrounding O-lines (defined by extrema of A_z) also exhibits a shift of the peak to higher T_e values than pdf of all cells, but the shift is smaller than that for X-lines; it has a positive skewness with higher pdf than that for all cells at high T_e. The result indicates the statistical importance of electron heating by reconnection.

The T_e evolution of reconnection current sheets is further examined to extract more quantitative results. For the single current sheet in Figure 2 (a-e), we analyze the fixed region shown in the plot with a size of 5 $d_i \times 10$ d_i. The average T_e over the fixed region at each time step increases over time (Figure 4a, blue), and the heating rate $\Delta T_e/m_i V_A^2$ increases from 7% at $t\omega_{ci} = 16.0$ to 21% at $t\omega_{ci} = 19.5$ (X-line first appears at $t\omega_{ci} = 16.5$). Here ΔT_e is the difference between the spatially averaged T_e and the simulation initial T_{e0}=0.05 (close to the value of the minimum T_e in the region), and V_A is the ion Alfvén speed based on the average n_e and |B| over the region at the instant time. T_e close to the X-line (averaged over 2 d_e × 2 d_e) is separately examined (Figure 4a, orange), which is usually greater than the ion-scale averaged T_e, while it occasionally may exhibit a decrease over time. The rate $\Delta T_e/m_i V_A^2$ close to the X-line is up to 30% (Figure 4b, orange). We note that the calculation of the heating rate has some differences from the typical way applied to reconnection studies [e.g., Phan et al., 2013; Shay et al., 2014], where ΔT_e is the difference between the outflow and inflow, and V_A is based on the density and the reconnecting component of the magnetic field in the inflow region. We applied the same method for some current sheets, where the outflow T_e is taken close to the X-line. The resulting heating rate varies over a larger range than those shown in Figure 4b, even for current sheets with simple structures, indicating more variability of heating in reconnection of such a turbulent environment. The complicated orientations and inhomogeneous inflow conditions lead to additional uncertainties when evaluating the heating rate. Therefore, we choose to use the presented method to avoid ambiguity, and the method is expected to be also applicable to 3D simulations and observations after minor modifications.

A statistical study of T_e evolution is performed using the superposed epoch analysis. We select 59 well isolated reconnection current sheets like that shown in Figure 2 (a-e) and 43 clusters of reconnection current sheets like in Figure 2f, 102 in total. Each single or cluster of current sheets is considered as one event, and we require at least one X-line in the event lasts for longer than 1

ω_{ci}^{-1}. For each event, we analyze a region with a fixed area, typically including a couple of d_i away from the current sheets like those shown in Figure 2. In cases where the X-line has significant displacements over time, the region for the analysis moves to capture the current sheet, while the area remains fixed. Figure 4c shows the superposed epoch analysis of the average T_e over the regions of each event. Each gray curve represents the time evolution of T_e for individual events. Epoch t=0 is defined as the time where X-line first appears, which is typically at $t\omega_{ci} = 16.0 \sim 17.0$. The red curve represents the median value of T_e over different events at each time; blue curves represent the 25% and 75% quartiles. Some reconnection events may not last as long as 3 ω_{ci}^{-1}, and the statistics at each time is only for the available events. In addition, we select 17 non-reconnection current sheets, where the maximum $|j_z|$ is greater than 3 times of standard deviation of $|j_z|$ in the entire simulation domain, but reconnection never occurs to form an X-line. The green curve shows the T_e evolution of these non-reconnection events during $t\omega_{ci} = 15.5 \sim 19.0$. It is clear that T_e of reconnection current sheets is greater than that of non-reconnection current sheets, and also increases over time. Figure 4d shows $\Delta T_e/m_i V_A^2$ that represents the heating rate by reconnection current sheets. Considering the range of 25%-75% quartiles, it increases from ~8% around the reconnection onset to 20%-30% at 3 ω_{ci}^{-1}, where both T_e and $\Delta T_e/m_i V_A^2$ start to approach to saturations. T_e close to the X-line (Figure 4c) exhibits a significant jump as reconnection starts, and statistically remains at steady values in the later time that are greater than the average T_e over a bigger region. The heating rate close to the X-line continues to increase from 10%-20% when reconnection starts to 25%-40% at 3 ω_{ci}^{-1}. The clearer increase of the heating rate than T_e in the later time indicates decrease of V_A and thus the reduction of the electromagnetic energy for reconnection.

The events included in the superposed epoch analysis cover about ¼ of the simulation domain. Later in time, the heated regions further spread as energized particles move around, and the entire simulation domain has a relatively smooth temperature of 0.1 m_ec^2, well represented by the saturation level of reconnection current sheets (Figure 4c).

4. Electron energization

Knowing that reconnection indeed contributes significant electron heating in the foreshock wave environment, we next investigate the electron energization mechanisms. First we will analyze the electron energy equations to see that $\boldsymbol{j_e} \cdot \boldsymbol{E}$ measures the electron energization, and the electron energization is dominant by the electron thermal energy gain. By taking the second-order moments of the Vlasov equation, we can obtain the energy equation of electrons, which can be further decomposed into the flow energy equation:

$$\frac{\partial u_{bulk,e}}{\partial t} + \nabla \cdot \boldsymbol{K_e} = \boldsymbol{j_e} \cdot \boldsymbol{E} - \boldsymbol{V_e} \cdot (\boldsymbol{\nabla} \cdot \boldsymbol{P_e}) \quad (1)$$

and thermal energy equation [e.g., Lu et al., 2018; Lapenta et al., 2020]:

$$\frac{\partial u_{th,e}}{\partial t} + \nabla \cdot \boldsymbol{H_e} + \boldsymbol{\nabla} \cdot \boldsymbol{q_e} = \boldsymbol{V_e} \cdot (\boldsymbol{\nabla} \cdot \boldsymbol{P_e}) \quad (2)$$

where $u_{bulk,e} = \frac{1}{2} m_e n_e V_e^2$ is the electron bulk flow energy density, $\boldsymbol{K_e} = \frac{1}{2} m_e n_e V_e^2 \boldsymbol{V_e}$ is the bulk flow energy flux, $\boldsymbol{j_e} = -n_e \boldsymbol{V_e}$ is the electron current density, $u_{th,e} = \frac{3}{2} n_e T_e$ is the thermal energy density, $\boldsymbol{H_e} = \boldsymbol{P_e} \cdot \boldsymbol{V_e} + u_{th,e} \boldsymbol{V_e}$ is the enthalpy flux, and $\boldsymbol{q_e} = m_e \int f |\boldsymbol{v} - \boldsymbol{V_e}|^2 (\boldsymbol{v} - \boldsymbol{V_e}) d^3 v$ is the heat flux. One way to understand equations (1) and (2) is to view the left-hand sides as the gain of flow or thermal energies, which includes both the temporal evolution of $u_{bulk,e}$ and $u_{th,e}$ in the specific region and the net energy flux across the region. It is a picture that typically applies to reconnection [e.g., Eastwood et al., 2013; Shay et al., 2014; Yamada et al., 2016;

Wang et al., 2018] and shocks [e.g., Schwartz et al., 1987; Schwartz et al., 2022], and usually the explicit time dependence can be further neglected in these situations. $\boldsymbol{j_e} \cdot \boldsymbol{E}$ represents the energy conversion from electromagnetic fields to electrons, and $\boldsymbol{V_e} \cdot (\boldsymbol{\nabla} \cdot \boldsymbol{P_e})$ alters the partition between flow and thermal energies. From the electron momentum equation, the electric field can be expressed as:

$$\boldsymbol{E} =- \boldsymbol{V_e} \times \boldsymbol{B} - \frac{1}{n_e e} \boldsymbol{\nabla} \cdot \boldsymbol{P_e} - \frac{m_e}{n_e e} \frac{d\boldsymbol{V_e}}{dt} \quad (3)$$

For electrons, the inertial term (last term in eq.(3)) is usually negligible due to its small mass (confirmed with our simulation data), so the non-ideal electric field in the electron bulk frame $\boldsymbol{E}' = \boldsymbol{E} + \boldsymbol{V_e} \times \boldsymbol{B}$ is dominated by $-\frac{1}{n_e e} \boldsymbol{\nabla} \cdot \boldsymbol{P_e}$. The energy conversion satisfies $\boldsymbol{j_e} \cdot \boldsymbol{E} = \boldsymbol{j_e} \cdot \boldsymbol{E}'$, while $\boldsymbol{V_e} \cdot (\boldsymbol{\nabla} \cdot \boldsymbol{P_e}) = \boldsymbol{j_e} \cdot (-\frac{1}{n_e e} \boldsymbol{\nabla} \cdot \boldsymbol{P_e})$. Thus, the two terms on the right-hand side of the flow energy equation (1) almost cancel with each other, indicating that the electron energization is dominated by the thermal energy gain. In observations of reconnection in the shock transition region, despite that the electron outflow jet is usually the clearest feature, the thermal energy gain should be the dominant form based on the above theoretical derivations.

More insights about the energization mechanisms can be obtained by decomposing $\boldsymbol{j_e} \cdot \boldsymbol{E}$:

$$\boldsymbol{j_e} \cdot \boldsymbol{E} = \boldsymbol{j}_{\boldsymbol{e}||} \cdot \boldsymbol{E}_{||} + \boldsymbol{j}_{\boldsymbol{e}\perp} \cdot \boldsymbol{E}_{\perp} \quad (3)$$

When electrons are mostly magnetized and the guiding center approximation is valid, the electron perpendicular drift can be decomposed as [e.g., Parker et al., 1957; Li et al., 2015]

$$\boldsymbol{j}_{\boldsymbol{e}\perp} =- ne \frac{\boldsymbol{E} \times \boldsymbol{B}}{B^2} + P_{e||} \frac{(\boldsymbol{B} \times \boldsymbol{\kappa})}{\boldsymbol{B^2}} + \frac{P_{e\perp}}{\boldsymbol{B^3}} (\boldsymbol{B} \times \boldsymbol{\nabla B}) - \left[\boldsymbol{\nabla} \times \frac{P_{e\perp} \boldsymbol{B}}{\boldsymbol{B^2}} \right]_{\perp} \quad (4)$$

representing the $\boldsymbol{E} \times \boldsymbol{B}$ drift, curvature drift, gradient-B drift, and magnetization drift, respectively, where the polarization drift has been neglected. Plugging it into equation (3), we get:

$$\boldsymbol{j_e} \cdot \boldsymbol{E} = \boldsymbol{j}_{e||} \cdot \boldsymbol{E}_{||} + P_{e||} \frac{(\boldsymbol{B} \times \boldsymbol{\kappa}) \cdot \boldsymbol{E}}{\boldsymbol{B}^2} + \frac{P_{e\perp}}{\boldsymbol{B}^3} (\boldsymbol{B} \times \boldsymbol{\nabla B}) \cdot \boldsymbol{E} - \left[\boldsymbol{\nabla} \times \frac{P_{e\perp}\boldsymbol{B}}{\boldsymbol{B}^2}\right]_{\perp} \cdot \boldsymbol{E} \quad (5)$$

The second term $P_{e||} \frac{(\boldsymbol{B} \times \boldsymbol{\kappa}) \cdot \boldsymbol{E}}{\boldsymbol{B}^2}$ represents Fermi acceleration. The third term $\frac{P_{e\perp}}{\boldsymbol{B}^3} (\boldsymbol{B} \times \boldsymbol{\nabla B}) \cdot \boldsymbol{E}$ represents Betatron acceleration. The last term is for the magnetization current $-\left[\boldsymbol{\nabla} \times \frac{P_{e\perp}\boldsymbol{B}}{\boldsymbol{B}^2}\right]_{\perp}$ that is associated with the collective gyro-motion in regions with inhomogeneous magnetic fields and pressure. The magnetization current can be further expressed as $-\frac{\nabla_{\perp} P_{e\perp} \times \boldsymbol{B}}{B^2} - P_{e\perp} \frac{(\boldsymbol{B} \times \boldsymbol{\kappa})}{\boldsymbol{B}^2} - \frac{P_{e\perp}}{\boldsymbol{B}^3} (\boldsymbol{B} \times \boldsymbol{\nabla B})$, where the first term is the diamagnetic current, the second term resembles the curvature drift by replacing $P_{e||}$ with $-P_{e\perp}$, and the third term cancels the gradient-B drift. Note that with some re-arrangements of the terms, we get $\boldsymbol{j}_{e\perp} = -ne \frac{\boldsymbol{E} \times \boldsymbol{B}}{B^2} - \frac{\nabla_{\perp} P_{e\perp} \times \boldsymbol{B}}{B^2} + (P_{e||} - P_{e\perp}) \frac{(\boldsymbol{B} \times \boldsymbol{\kappa})}{\boldsymbol{B}^2}$ [e.g., Zelenyi et al., 2004; Hwang et al., 2021], so the net drifts that can contribute to $\boldsymbol{j_e} \cdot \boldsymbol{E}$ (i.e., except for the $\boldsymbol{E} \times \boldsymbol{B}$ drift) are the diamagnetic drift and the curvature-related drift if an anisotropy exists, while the gradient-B drift of particles (i.e., Betatron mechanism) does not have a net contribution to the fluid. The way of decomposition in equation (4) is still valuable, since it distinguishes the drifts related to the guiding center motion (curvature, gradient-B drifts) and those related to gyrations around the magnetic field (magnetization drift). It also helps understand how representative particles with the thermal energy can be energized through the Fermi and Betatron mechanisms.

The profiles of individual terms in equation (5) for the example single current sheet (Figure 2 top) when X-line first appears are shown in Figure 5 (top). Such decomposition is based on the guiding center approximation, so it only applies to regions where the local $\mathrm{K} = \sqrt{(R_C/r_g)} > 1$, where $\mathrm{R_C}$ is the magnetic curvature radius, and $\mathrm{r_g}$ is the electron thermal gyro-radius. At the shown time, the guide field for reconnection at the X-line is about 60% of the reconnecting magnetic field in the inflow region, and the entire presented region satisfies $\mathrm{K} > 1$. Strong $\boldsymbol{j}_{\boldsymbol{e}||} \cdot \boldsymbol{E}_{||}$ shows up (Figure 5a), with predominantly positive values in the X-line vicinity and bipolar structures along the separatrices, which are consistent with electron holes and lead to segments of $\mathrm{T_e}$ enhancements (Figure 2c, enhancements confirmed to be in the $\mathrm{T_{e||}}$ component). $\boldsymbol{j}_{\boldsymbol{e}\perp} \cdot \boldsymbol{E}_{\perp}$ is weaker than $\boldsymbol{j}_{\boldsymbol{e}||} \cdot \boldsymbol{E}_{||}$ at the X-line, but has strong enhancements in the reconnection exhaust only a few $\mathrm{d_e}$ downstream of the X-line. Decomposing $\boldsymbol{j}_{\boldsymbol{e}\perp} \cdot \boldsymbol{E}_{\perp}$, the strongest enhancement is in the Fermi term in the reconnection exhaust, while some negative values appear; the Betatron term is much weaker, with some localized enhancements downstream of the region with strong Fermi contributions; the magnetization term has moderate enhancements throughout the region, including positive contributions around the X-line.

To evaluate the net contributions of different mechanisms, we examine the integrated $\boldsymbol{j}_{\boldsymbol{e}} \cdot \boldsymbol{E}$ over the region at different time steps. The total $\boldsymbol{j}_{\boldsymbol{e}} \cdot \boldsymbol{E}$ (Figure 5f) is strongest at the start of reconnection ($t\omega_{ci} = 16.5$) and decreases at later time. $\boldsymbol{j}_{\boldsymbol{e}||} \cdot \boldsymbol{E}_{||}$ dominates before and near the reconnection onset ($t\omega_{ci} = 16.0 - 16.5$), $\boldsymbol{j}_{\boldsymbol{e}\perp} \cdot \boldsymbol{E}_{\perp}$ peaks and dominates at $t\omega_{ci} = 17.0$. The decomposition of $\boldsymbol{j}_{\boldsymbol{e}\perp} \cdot \boldsymbol{E}_{\perp}$ is shown in Figure 5g, where the 'demagnetized' term (cyan) represents $\boldsymbol{j}_{\boldsymbol{e}\perp} \cdot \boldsymbol{E}_{\perp}$ in regions with $\mathrm{K} < 1$, and other terms are integrated over regions with $\mathrm{K} > 1$. The demagnetized term turns out to have a much smaller amplitude than other terms for all the events. The sum of four terms (green) overall agrees with $\boldsymbol{j}_{\boldsymbol{e}\perp} \cdot \boldsymbol{E}_{\perp}$ (blue in Figure 5f), and the difference is mainly attributed to numerical uncertainties, with minor contributions by the imperfect assumptions like gyrotropic pressure tensors. At the early time near the reconnection onset, the net Fermi contribution is negative, and the magnetization term contributes most positive values. Later the Fermi term becomes the dominant mechanism to contribute positive energization. The Betatron term contributes small positive values in most of the interval.

A superposed epoch analysis is performed to examine the energization mechanisms for the 102 events, and the trend is mostly consistent with the example shown in Figure 5. $<\boldsymbol{j_e}\cdot\boldsymbol{E}>$ shown in Figure 6a is the average value per unit area, so that results in different events can be compared. The following panels show the percentage of each term with respect to $<\boldsymbol{j_e}\cdot\boldsymbol{E}>$. $<\boldsymbol{j_e}\cdot\boldsymbol{E}>$ tends to be the strongest near the start of the reconnection, and the values before t=0 is already comparable to those at t=0. Figure 6b-6e show the percentage contributions of different terms with respect to $<\boldsymbol{j_e}\cdot\boldsymbol{E}>$. The contribution by $E_{\parallel}$ (Figure 6b) has a slight decreasing trend over time, where the median value is above 50% at the early time and below 50% later. For the decomposition of $\boldsymbol{j_{e\perp}}\cdot\boldsymbol{E_{\perp}}$, at the later time, the relative importance is consistent with the laminar reconnection studies [e.g., Dahlin et al., 2014, 2015, 2016; Li et al., 2015, 2017]: the Fermi term (Figure 6c) dominates the positive contribution, and the Betatron term (Figure 6d) is negative. The features at the earlier time are different, where the Fermi term is negative, the median value of the Betatron term can be slightly positive before reconnection starts, and the magnetization term (Figure 6e) dominates the positive contribution. We may visualize that as the current sheet thins down and reconnection is initiated, it creates a highly inhomogeneous environment to weakly 'demagnetize' electrons, though the gradient scales are not large enough to fully demagnetize electrons and invalidate the guiding center approximation. The collective gyrations of particles contribute the net current and lead to energizations, manifested as the contribution by the magnetization term.

We look into more details about how the Fermi term appears to be negative values. Mathematically, the Fermi term $P_{e||}\frac{(\boldsymbol{B}\times\boldsymbol{\kappa})\cdot\boldsymbol{E}}{\boldsymbol{B}^2}$ can be re-arranged into $P_{e||}(\boldsymbol{V}_{\boldsymbol{E}\times\boldsymbol{B}}\cdot\boldsymbol{\kappa})$. Therefore, in the reconnection exhaust where both the magnetic curvature and the $\boldsymbol{E}\times\boldsymbol{B}$ outflow velocity point away from the X-line in the reconnection (x-y) plane, the Fermi term is expected to be positive. However, in the ion diffusion region (or electron-only reconnection) where ions and electrons are decoupled, Hall fields develop, where electrons that are roughly frozen-in drag magnetic field lines toward the out-of-plane direction to form the quadrupolar Hall magnetic field [e.g., Mandt et al., 1994]. As illustrated in Figure 7a, the out-of-plane component of the magnetic curvature is opposite to the $\boldsymbol{E}\times\boldsymbol{B}$ drift, resulting in negative values of the Fermi term. Figure 7 shows the decomposition of the Fermi term for the example single reconnection current sheet, where Figures 7b-7e are for $t\omega_{ci}=16.5$ when the net Fermi term is negative, and Figures 7f-7i are for $t\omega_{ci}=17.0$ when the net Fermi term is positive (Figure 5g). At $t\omega_{ci}=16.5$, the guide field B_z in the current layer is negative (Figure 7b). The Fermi term (Figure 7c) is decomposed into the in-plane $Fermi_{xy}$ (Figure 7d) and out-of-plane $Fermi_z$ (Figure 7e) components ($Fermi=Fermi_{xy}+Fermi_z$). $Fermi_{xy}$ exhibits strong positive values in the exhaust as expected, and some negative values appear in the inflow region and some regions further away from the X-line. $Fermi_z$ is mostly negative, consistent with the Hall pattern. At $t\omega_{ci}=17.0$, B_z becomes positive in the current sheet, and the quadrupolar Hall feature becomes clearer (Figure 7f). The positive values in $Fermi_{xy}$ (Figure 7g) extend to further distances from the X-line as the exhaust expands, while Fermi$_z$ (Figure 7h) exhibits strong negative values around the B_z reversal regions.

The superposed epoch analysis of the Fermi term (per unit area) for all selected reconnection current sheets is presented in Figure 8. The net Fermi term has the median value changing from negative to positive values over time (Figure 8a). Fermi$_{xy}$ is negative before reconnection starts and the median value crosses zero at t=0 (Figure 8b). Fermi$_z$ remains at negative values for longer time up to $\Delta t\omega_{ci}$~1 (Figure 8c). It also reverses to positive values later, and the examinations of individual events reveal that the positive Fermi$_z$ is associated with complicated structures far away from the X-line, irrelevant to the Hall structures.

The analysis suggests a process that around the onset of reconnection, Fermi contributes negative values associated with the electron dragging of field lines, which occurs in the out-of-plane directions due to the Hall effect, as well as in the in-plane components such as in the inflow region. As reconnection develops and the exhaust region expands, the aligned outflow and magnetic curvature in the reconnection plane dominates, leading to positive Fermi contributions.

5. Discussions

The investigations above have demonstrated the importance of magnetic reconnection on electron heating in the foreshock environment, and have revealed the bulk electron energization mechanisms. Through the analysis, we can try to build a picture of the evolution of electron energization. Figure 9 shows the correlation coefficient between filtered fields of the magnetic field strength (dB) and electron temperature (dT_e) at different spatial scales. The results at $t\omega_{ci}$ =

17.0 are shown, when an increasing number of X-lines start to appear, and the features are consistent over a few ω_{ci}^{-1}. At large scales of $kd_i \lesssim 0.7$, dB and dT_e exhibit positive correlations with coefficients of ~0.4 (the coefficient at earlier time can be higher up to ~0.8), consistent with adiabatic heating where T_e increases as the magnetic field compresses. At small scales of $kd_i \gtrsim 0.7$, dB and dT_e no longer have good positive correlations, and the coefficient is slightly negative. It reflects that in sub-ion scale structures, electrons tend to be heated in low-field regions such as the reconnection current sheets. Such a feature of electron heating at large and small scales summarizes a consistent picture with the examples we examined (e.g., Figure 2a-2c).

Since we have found that the reconnection current sheets produce more electron heating than non-reconnection current sheets, what is the difference between the two? By examining individual cases, we found that a main difference seems to be the current sheet thickness. We selected 93 reconnection current sheets to calculate their smallest thicknesses, which include the single X-line events used in the above statistics and additional current sheets that are well isolated from others when their thicknesses reach the minimum. The thickness is determined as the full width half maximum of $|j_z|$ in the cut along N across the X-line. The thickness is plotted as a function of the maximum $|j_z|$ (j_{max}) in Figure 10, which lies in the range of 1~5 d_e for reconnection current sheets (black) with a median value of 2.4 d_e. The cyan dots show the thicknesses for 17 non-reconnection current sheets, which is overall greater than those of reconnection current sheets, with a median value of 4.3 d_e. Some non-reconnection current sheets have the thickness reaching the group of reconnection current sheets around 3 d_e; however, we find that they stay at such thin scales only briefly at one time step, while the reconnection current sheets hold the small thickness for longer time. The quantitative result demonstrates the difference in thickness between reconnection and non-reconnection current sheets. It suggests that driving the current sheet to a thin scale for sufficient time is a necessary condition for initiating reconnection, and it seems to be also a sufficient condition in the presented simulation.

6. Conclusions

We have investigated electron heating associated with magnetic reconnection in foreshock waves using a 2D PIC simulation that starts from the ion-ion beam instability. Reconnection develops as the ion-scale waveform distorts to form electron-scale current sheets. We obtain main conclusions regarding the electron heating and energization mechanisms:

(1) T_e is statistically higher close to the reconnection X-line than elsewhere, directly demonstrating the importance of reconnection in heating electrons in such an environment. The statistical analysis of the T_e evolution in individual current sheets shows that T_e in reconnection current sheets is greater than that in non-reconnection current sheets and increases over time for the time scale of a couple ω_{ci}^{-1}. Using $\Delta T_e/(m_i V_{Ai}^2)$ to represent the heating rate, where the parameters are based on the values averaged over a few d_i that covers the whole current sheet, it is about 20%-30% at the near-saturation level. The heating rate at the X-line is 10%-20% at the start of reconnection and increases to 25%-40% at saturation.

(2) The bulk electron energization by reconnection is analyzed by decomposing $\boldsymbol{j_e} \cdot \boldsymbol{E}$ with the guiding center approximation. $E_{||}$ statistically contributes more than 50% of the energization around the onset of reconnection and drops to lower than 50% later, and it is in the form of both reconnection electric field near the X-line and intense bipolar electron holes that usually develop

before reconnection starts. For $\boldsymbol{E}_\perp$ contributions, the energization at a couple ω_{ci}^{-1} after reconnection onset is dominant by the Fermi mechanism. At earlier time close to the reconnection onset, the perpendicular energization is dominant by the magnetization term associated with the gyro-motion in the inhomogeneous fields. Meanwhile, the Fermi term first has a net negative contribution and a positive contribution later. A primary contribution to the negative Fermi values is the Hall effect where electrons drag field lines in the out-of-plane direction to form the Hall magnetic field. As reconnection evolves and expands, the positive Fermi terms in the reconnection plane associated with the outflow gradually dominates over the negative Hall contribution.

We note that although the electron energization is through $\boldsymbol{j_e} \cdot \boldsymbol{E}$ and the energization mostly goes to the thermal energy gain, the enhancements of $\boldsymbol{j_e} \cdot \boldsymbol{E}$ and T_e are not correlated in the point-wise sense. The thermal energy gain consists of a more complicated definition of $\frac{\partial u_{th,e}}{\partial t} + \nabla \cdot \boldsymbol{H_e} + \boldsymbol{\nabla} \cdot \boldsymbol{q_e} > 0$. In addition to the T_e enhancement, the compression associated with n and V_e enhancements and the temporal variations (demonstrated to be non-negligible in Figure 4) can also contribute to balance $\boldsymbol{j_e} \cdot \boldsymbol{E}$. That's why we examine $\boldsymbol{j_e} \cdot \boldsymbol{E}$ and T_e separately, and it is reasonable to see lack of simultaneous enhancements of the two during in situ observations.

The characteristics of the reconnection current sheets in the simulation help us understand the features that may be difficult to interpret in observations. One interesting feature common to the current sheets in this simulation is that electrons exhibit shear flows along L, which originates from the flow along the ion-scale wave field and later evolves into part of the reconnection outflow jet (e.g., Figure 2e). The shear flow is sizable: for the reconnection current sheets we examine, the median value of shear flow amplitude at the minimum current sheet thickness is 5.5 $V_{A,asym}$. In addition, in such a turbulent environment, reconnection current sheets develop as clusters. The outflow regions of some current sheets can be the inflow regions of others, and particles can get continuous energization by moving through multiple reconnection sites. It leads to complicated current sheet structures and complicated profiles of quantities like V_e and T_e, which cannot be understood as the result of a single reconnection event. At least based on the result of the presented simulation, reconnection is likely to occur once the current sheet can be driven to small thicknesses. It reminds us that when analyzing observation data, current sheets that have structures inconsistent with the most standard reconnection may still be reconnecting or will reconnect later, and the interactions between multiple current sheets likely affect the structures. The heating and energization in reconnection in the shock transition region like the foreshock waves need further investigations in observations, which can be compared with the simulation results and will probably reveal more interesting facts beyond those in 2D simulations.

Acknowledgments

The simulation data presented in the paper are available at https://zenodo.org/record/7178188#.ZFW8KnZBy5c

References

Akimoto, K., Winske, D., Gary, S. P., & Thomsen, M. F. (1993). Nonlinear evolution of electromagnetic ion beam instabilities. Journal of Geophysical Research, 98(A2), 1419–1433. https://doi.org/10.1029/92JA02345

Bandyopadhyay, R., Chasapis, A., Matthaeus, W., et al. (2021), Energy dissipation in turbulent reconnection, Phys. Plasmas, 28, 112305, doi: 10.1063/5.0071015

Bowers, K. J., Albright, B. J., Bergen, B., Yin, L., Barker, K. J., and Kerbyson, D. J., "0.374 Pflop/s trillion-particle kinetic modeling of laser plasma interaction on roadrunner," in Proceedings of the 2008 ACM/IEEE Conference on Supercomputing, SC'08 (IEEE Press, Piscataway, NJ, 2008), pp. 63:1–63:11.

Chen, L. J., Wang, S., Ng, J., Bessho, N., Tang, J. M., Fung, S. F., et al. (2021). Solitary magnetic structures at quasi-parallel collisionless shocks: Formation. Geophysical Research Letters, 48, e2020GL090800. https://doi.org/10.1029/2020GL090800

Chen, L.-J., Halekas, J., Wang, S., DiBraccio, G. A., Romanelli, N., Ng, J., et al. (2022). Solitary magnetic structures developed from gyro-resonance with solar wind ions at Mars and Earth. Geophysical Research Letters, 49, e2021GL097600. https://doi.org/10.1029/2021GL097600

Dahlin, J. T., J. F. Drake, and M. Swisdak (2014), The mechanisms of electron heating and acceleration during magnetic reconnection Phys. Plasmas 21, 092304, doi: 10.1063/1.4894484

Dahlin, J. F. Drake, and M. Swisdak (2015), Electron acceleration in three-dimensional magnetic reconnection with a guide field, Phys. Plasmas 22, 100704, doi: 10.1063/1.4933212

Dahlin, J. F. Drake, and M. Swisdak (2016), Parallel electric fields are inefficient drivers of energetic electrons in magnetic reconnection, Phys. Plasmas, 23, 120704, doi: 10.1063/1.4972082

Doss, C. E., C. M. Komar, P. A. Cassak, F. D. Wilder, S. Eriksson, and J. F. Drake (2015), Asymmetric magnetic reconnection with a flow shear and applications to the magnetopause, J. Geophys. Res. Space Physics, 120, 7748–7763, doi:10.1002/2015JA021489.

Eastwood, J. P., E. A. Lucek, C. Mazelle, K. Meziane, Y. Narita, J. Pickett, and R. Treumann (2005), The foreshock, Space Sci. Rev., 118, 41–94.

Eastwood, J. P., Phan, T. D., Drake, J. F., Shay, M. A., Borg, A. L., Lavraud, B., & Taylor, M. G. G. T. (2013). Energy partition in magnetic reconnection in Earth's magnetotail. Physical Review Letters, 110(22), 225001. https://doi.org/10.1103/PhysRevLett.110.225001

Gingell, I., Schwartz, S. J., Eastwood, J. P., Burch, J. L., Ergun, R. E., Fuselier, S., et al. (2019). Observations of magnetic reconnection in the transition region of quasi-parallel shocks. Geophysical Research Letters, 46, 1177–1184. https://doi.org/10.1029/2018GL081804

Gingell I., Schwartz, S. T., Eastwood, J. P., Stawarz, J. E., Burch, J. L., Ergun, R. E., et al. (2020). Statistics of reconnecting current sheets in the transition region of earth's bow shock. Journal of Geophysical Research: Space Physics, 125, e2019JA027119. https://doi.org/10.1029/2019JA027119

Haggerty,C. C., T. N. Parashar, W. H. Matthaeus, M. A. Shay, Y. Yang, M. Wan, P. Wu, and S. Servidio, "Exploring the statistics of magnetic reconnection x-points in kinetic particle-in-cell turbulence," Phys. Plasmas 24, 102308, https://doi.org/10.1063/1.5001722

Hwang K-J, Dokgo K, Choi E, Burch JL, Sibeck DG, Giles BL, Norgren C, Nakamura TKM, Graham DB, Khotyaintsev Y, Shi QQ, Gershman DJ, Pollock CJ, Ergun RE, Torbert RB, Russell CT and Strangeway RJ (2021) Bifurcated Current Sheet Observed on the Boundary of Kelvin-Helmholtz Vortices. Front. Astron. Space Sci. 8:782924. doi: 10.3389/fspas.2021.782924

Li, X., F. Guo, H. Li, and G. Li (2015), NONTHERMALLY DOMINATED ELECTRON ACCELERATION DURING MAGNETIC RECONNECTION IN A LOW-β PLASMA Astrophys. J. Lett. 811, L24, doi:10.1088/2041-8205/811/2/L24

Li, Xiaocan, Fan Guo, Hui Li, and Gang Li (2017), Particle Acceleration during Magnetic Reconnection in a Low-beta Plasma, The Astrophys. J., 843:21, https://doi.org/10.3847/1538-4357/aa745e

Liu, T. Z., Lu, S., Turner, D. L., Gingell, I., Angelopoulos, V., Zhang, H., et al. (2020). Magnetospheric Multiscale (MMS) observations of magnetic reconnection in foreshock transients. Journal of Geophysical Research: Space Physics, 125, e2020JA027822. https://doi.org/10.1029/2020JA027822

Mandt, M. E., Denton, R. E., & Drake, J. F. (1994). Transition to whistler mediated magnetic reconnection. Geophysical Research Letters, 21(1), 73–76. https://doi.org/10.1029/93gl03382

Parker, E. N. (1957), Newtonian Development of the Dynamical Properties of Ionized Gases of Low Density, Phys. Rev. Lett., 107, 924

Phan, T. D., M. A. Shay, J. T. Gosling, M. Fujimoto, J. F. Drake, G. Paschmann, M. Oieroset, J. P. Eastwood, and V. Angelopoulos (2013), Electron bulk heating in magnetic reconnection at Earth's magnetopause: Dependence on the inflow Alfvén speed and magnetic shear, Geophys. Res. Lett., 40, doi:10.1002/grl.50917.

Phan, T. D., J. P. Eastwood, M. A. Shay, J. F. Drake, B. U. Ö. Sonnerup, M. Fujimoto, P. A. Cassak, M. Øieroset, J. L. Burch, R. B. Torbert, A. C. Rager, J. C. Dorelli, D. J. Gershman, C. Pollock, P. S. Pyakurel, C. C. Haggerty, Y. Khotyaintsev, B. Lavraud, Y. Saito, M. Oka, R. E. Ergun, A. Retino, O. L. Contel, M. R. Argall, B. L. Giles, T. E. Moore, F. D. Wilder, R. J. Strangeway, C. T. Russell, P. A. Lindqvist, and W. Magnes (2018), "Electron magnetic reconnection without ion coupling in Earth's turbulent magnetosheath," Nature 557, 202–206, doi: 10.1038/s41586-018-0091-5

Qi, Y., Li, T. C., Russell, C. T., Ergun, R. E., Jia, Y.-D., & Hubbert, M. (2022). Magnetic flux transport identification of active reconnection: MMS observations in earth's magnetosphere. The Astrophysical Journal Letters, 926(2), L34. https://doi.org/10.3847/2041-8213/ac5181

Schwartz, S. J., Thomsen, M. F., Feldman, W. C., and Douglas, F. T. (1987), Electron dynamics and potential jump across slow mode shocks, J. Geophys. Res., 92(A4), 3165– 3174, doi:10.1029/JA092iA04p03165.

Schwartz, S. J., Burgess, D., Wilkinson, W. P., Kessel, R. L., Dunlop, M., & Luehr, H. (1992). Observations of short large-amplitude magnetic structures at a quasi-parallel shock. Journal of Geophysical Research, 97(A4), 4209–4227. https://doi.org/10.1029/91JA02581

Schwartz, S. J., Goodrich, K. A., Wilson, L. B., Turner, D. L., Trattner, K. J., Kucharek, H., et al. (2022). Energy partition at collisionless supercritical quasiperpendicular shocks. Journal of Geophysical Research: Space Physics, 127, e2022JA030637. https://doi.org/10.1029/2022JA030637

Shay, M. A., Haggerty, C. C., Phan, T. D., Drake, J. F., Cassak, P. A., & Wu, P., et al. (2014). Electron heating during magnetic reconnection: A simulation scaling study. Physics of Plasmas, 21(12), 122902. https://doi.org/10.1063/1.4904203

M. A. Shay, C. C. Haggerty, W. H. Matthaeus, T. N. Parashar, M. Wan, and P. Wu (2018), Turbulent heating due to magnetic reconnection, Phys. Plasmas 25, 012304, https://doi.org/10.1063/1.4993423

Stawarz, J. E., Eastwood, J. P., Phan, T. D., Gingell, I. L., Pyakurel, P. S., Shay, M. A., et al. (2022). Turbulence-driven magnetic reconnection and the magnetic correlation length: Observations from Magnetospheric Multiscale in Earth's magnetosheath. Physics of Plasmas, 29(1), 012302. https://doi.org/10.1063/5.0071106

Voros, Z., Yordanova, E., Varsani, A., Genestreti, K. J., Khotyaintsev, Y. V., Li, W.,⋯Saito, Y. (2017). MMS observation of magnetic reconnection in the turbulent magnetosheath. Journal of Geophysical Research: Space Physics, 122, 11,442 – 11,467. https://doi.org/10.1002/2017JA024535

Wang, S., Chen, L.-J., Bessho, N., Hesse, M., Yoo, J., Yamada, M., et al. (2018). Energy conversion and partition in the asymmetric reconnection diffusion region. Journal of Geophysical Research: Space Physics, 123, 8185–8205. https://doi.org/10.1029/2018JA025519

Wang, S., Chen, L.-J., Bessho, N., Hesse, M., Wilson, L. B., Giles, B., et al. (2019). Observational evidence of magnetic reconnection in the terrestrial bow shock transition region. Geophysical Research Letters, 46, 562–570. https://doi.org/10.1029/2018GL080944

Wang, L.-J. Chen, N. Bessho, M. Hesse, L. B. Wilson III, R. Denton, J. Ng, B. Giles, R. Torbert, and J. Burch (2020), " Ion-scale current structures in short largeamplitude magnetic structures," Astrophys. J. 898, 121, doi: 10.3847/1538-4357/ab9b8b

Wilder, F. D., Conley, M., Ergun, R. E., Newman, D. L., Chasapis, A., Ahmadi, N., et al. (2022). Magnetospheric multiscale observations of waves and parallel electric fields in reconnecting current sheets in the turbulent magnetosheath. Journal of Geophysical Research: Space Physics, 127, e2022JA030511. https://doi.org/10.1029/2022JA030511

Wilson, L. B., III (2016), Low frequency waves at and upstream of collisionless shocks, in Low-frequency Waves in Space Plasmas, Geophys. Monogr. Ser., vol. 216, edited by A. Keiling, D.-H. Lee, and V. Nakariakov, pp. 269–291, AGU, Washington, D. C., doi:10.1002/9781119055006.ch16.

Yamada, M., Yoo, J., & Myers, C. E. (2016). Understanding the dynamics and energetics of magnetic reconnection in a laboratory plasma: Review of recent progress on selected fronts. Physics of Plasmas, 23(5), 055402. https://doi.org/10.1063/1.4948721

Zelenyi, L. M.,Malova, H. V., Popov, V. Y., Delcourt, D., Sharma, A. S., and Foss, S. (2004). Nonlinear Equilibrium Structure of Thin Currents Sheets: Influence of Electron Pressure Anisotropy. Nonlin. Process. Geophys. 11, 579–587. doi:10.5194/npg-11-579-2004

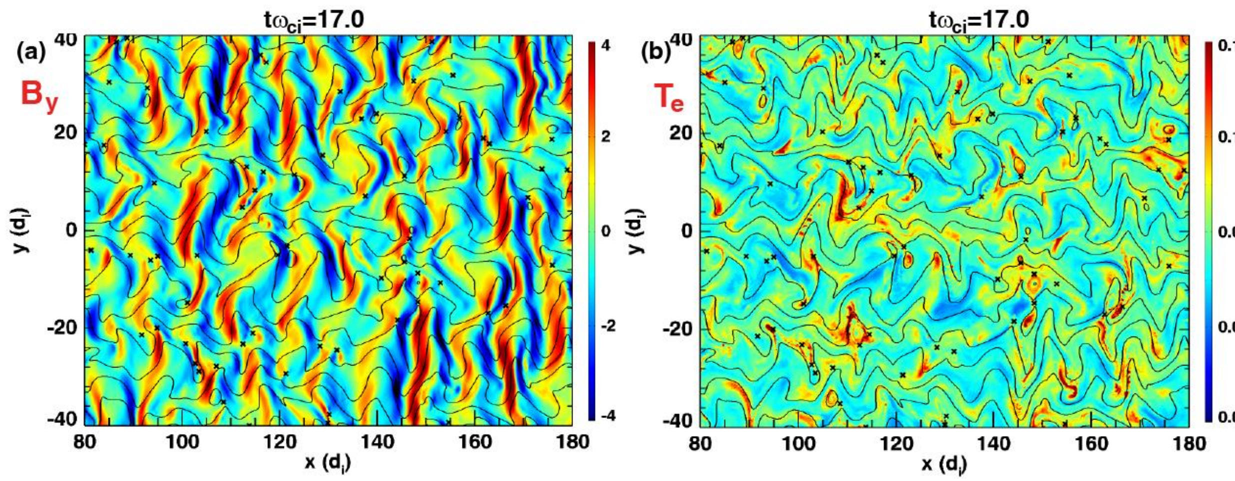

Figure 1. Overview of the simulation. (a) B_y. The vertical stripes are the wave fields from the ion-ion instability, which have been distorted to form current sheets. (b) T_e, which tend to exhibit enhancements in current sheets with sharp bending of field lines (overplotted black curves). The 'X' symbols mark the X-line locations.

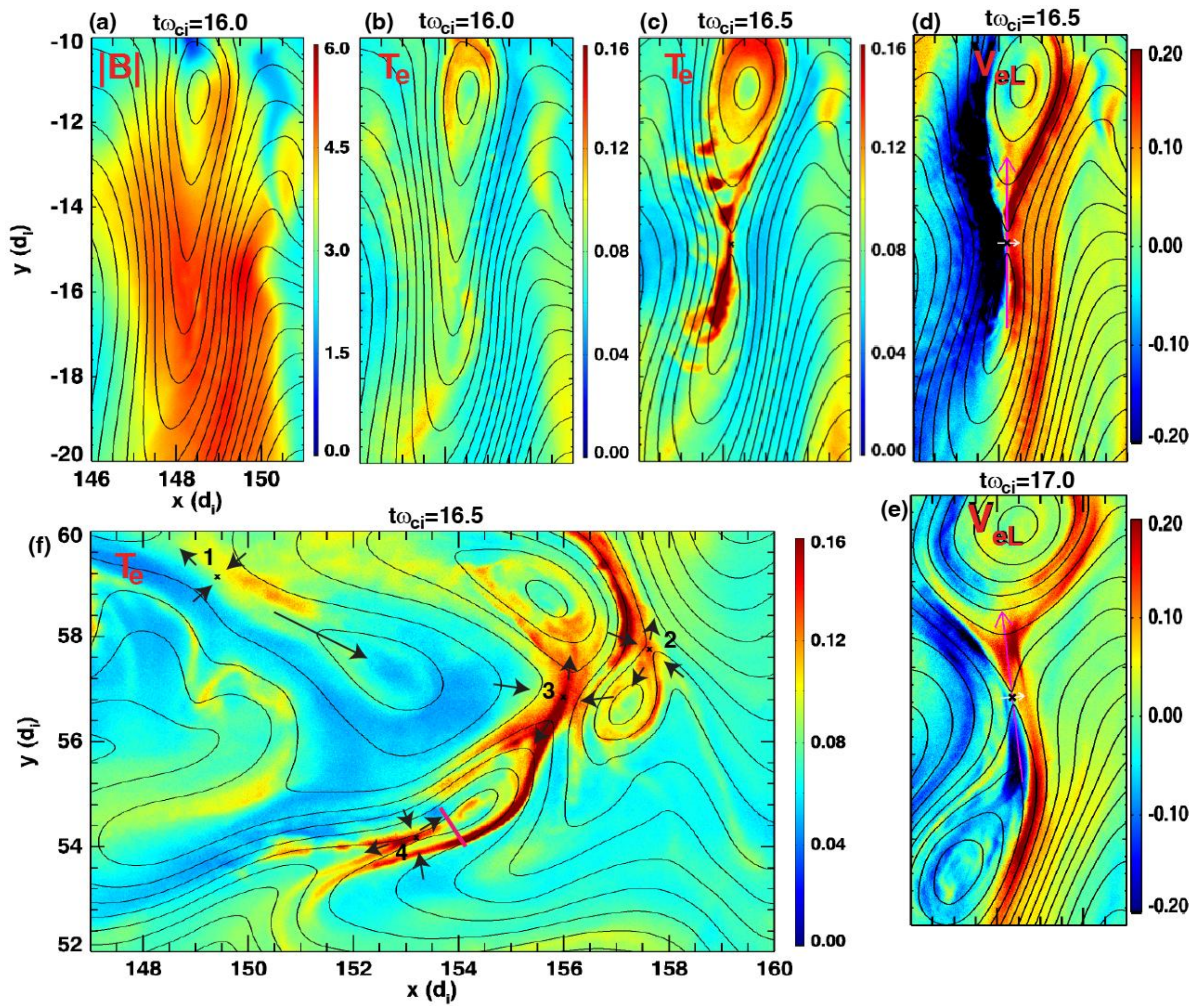

Figure 2. Example reconnection current sheets. (a)-(e) Evolution of an isolated current sheet with the time labelled on top of the panels. (a) Magnetic field amplitude |B|, (b)-(c) T_e showing enhancements in the reconnection current sheet. (d)-(e) Electron velocity along L (V_{eL}) showing a shear flow that evolves into reconnection outflow jets. The magenta and white arrows indicate the L and N directions, respectively. (f) T_e in an example cluster of multiple X-lines. Arrows indicate the inflow and outflow directions of each X-line. It shows the interaction between different reconnection sites.

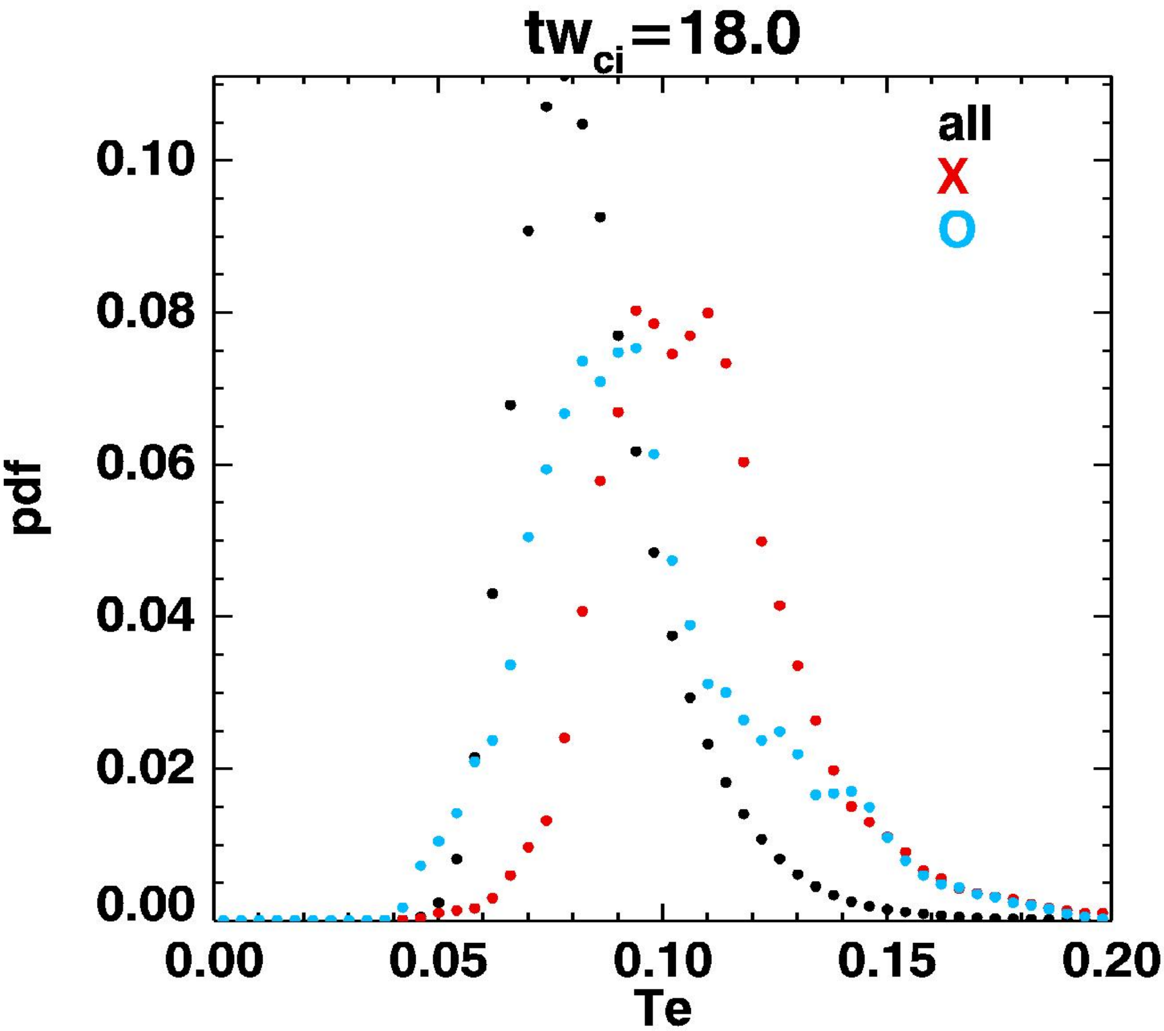

Figure 3. The probability distribution function of T_e at $t\omega_{ci} = 18.0$ with a maximum number of X-lines. Black dots are for all grids in the simulation. Red dots are for grids in 2 d_e × 2 d_e surrounding X-lines, where the distribution shifts to higher T_e. Cyan dots are for grids surrounding O-lines, where the distribution also shifts to higher T_e compared to the black distribution but not as much as the red distribution near X-lines.

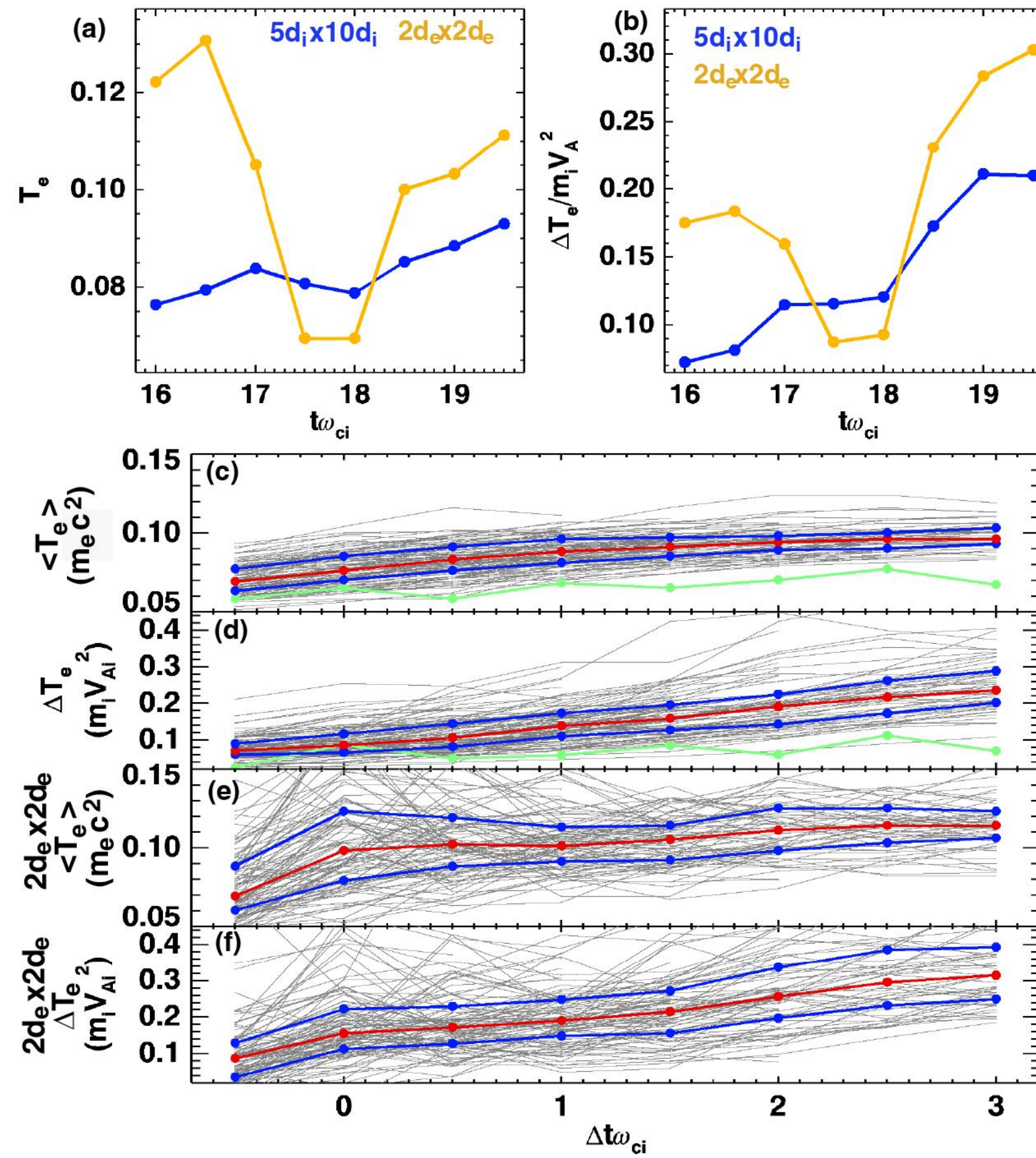

Figure 4. T_e evolution in reconnection current sheets. (a)-(b) T_e evolution over time in the example single current sheet shown in Figure 2 (top). The blue curves represent the average T_e over 5 d_i × 10 d_i that covers the whole current sheet, and orange curves represent the average T_e over 2 d_e × 2 d_e surrounding X-lines. (a) T_e in unit of m_ec^2; (b) heating rate $\Delta T_e/(m_i V_A^2)$, where ΔT_e is the average T_e subtracted by the initial T_e=0.05 m_ec^2, and V_A is based on the average n and |B| over the 5 d_i × 10 d_i region. (c)-(f) Superposed epoch analysis of T_e for 102 events of single or clusters of reconnection current sheets. Epoch t=0 is when the X-line first appears. Gray: curves for individual events; red: median values; blue: 25% and 75% quantiles. (c) average T_e over the d_i-scale region covering the current sheets, and the corresponding heating rate is in (d); (e) average T_e over 2 d_e × 2 d_e surrounding X-lines, and the corresponding heating rate is in (f). The green curve in (c)-(d) are the median values for 17 non-reconnection current sheets. The result shows clear electron heating in reconnection current sheets that increases over time, and the heating rate is 10%~40%.

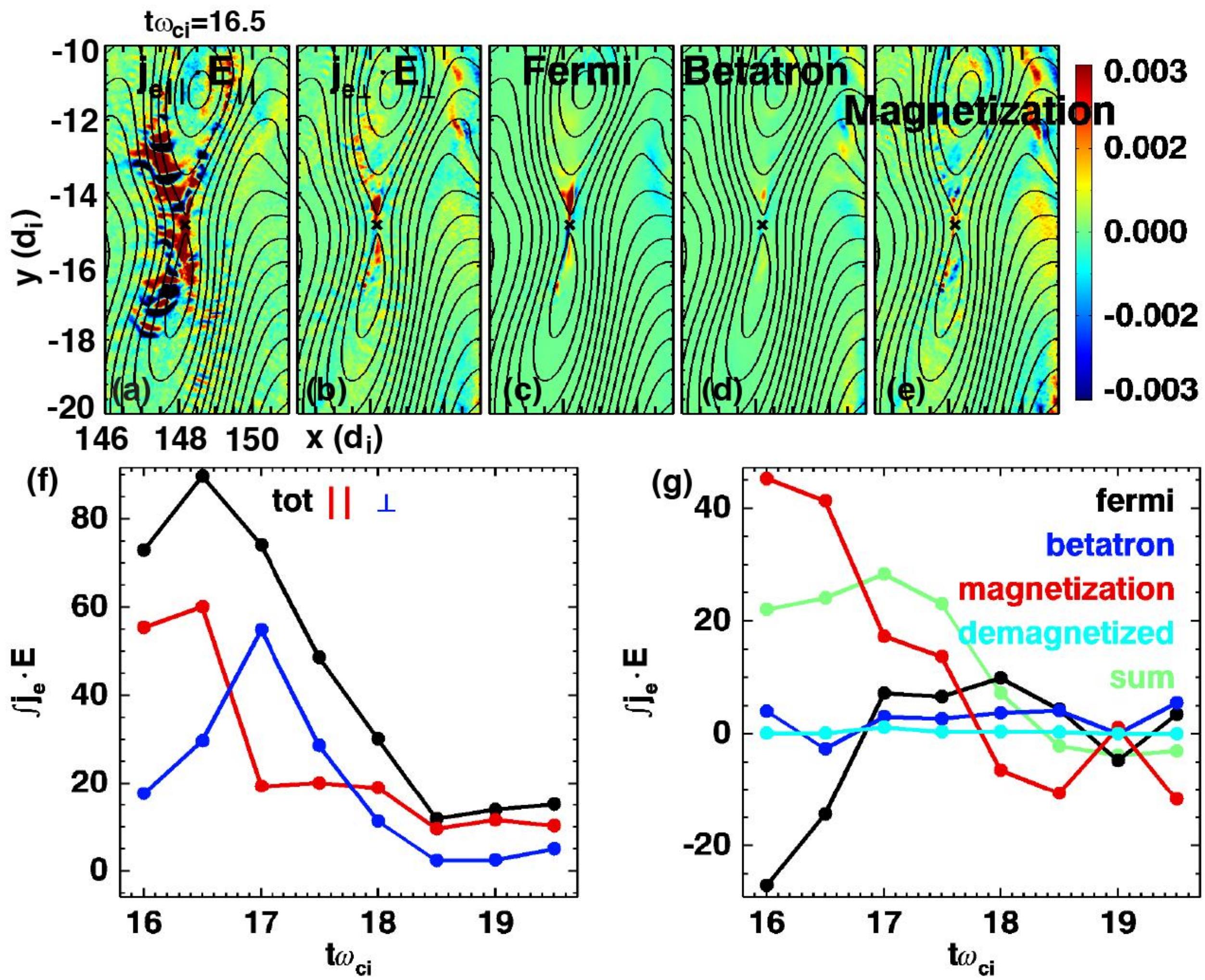

Figure 5. Electron energization represented by $\boldsymbol{j_e} \cdot \boldsymbol{E}$ decomposition for the example single current sheet in Figure 2 (top). (a)-(e) Profiles of decomposed terms at the time when the X-line first appears. (f) The integrated $\boldsymbol{j_e} \cdot \boldsymbol{E}$ over the shown region at different time steps, and the decomposition into the parallel and perpendicular components. (g) Decomposition of $\boldsymbol{j_{e\perp}} \cdot \boldsymbol{E_\perp}$, where 'demagnetized' represents $\boldsymbol{j_{e\perp}} \cdot \boldsymbol{E_\perp}$ in regions with $\mathrm{K} < 1$, and other terms are calculated over regions with $\mathrm{K} > 1$; 'sum' is the summation of the other four terms.

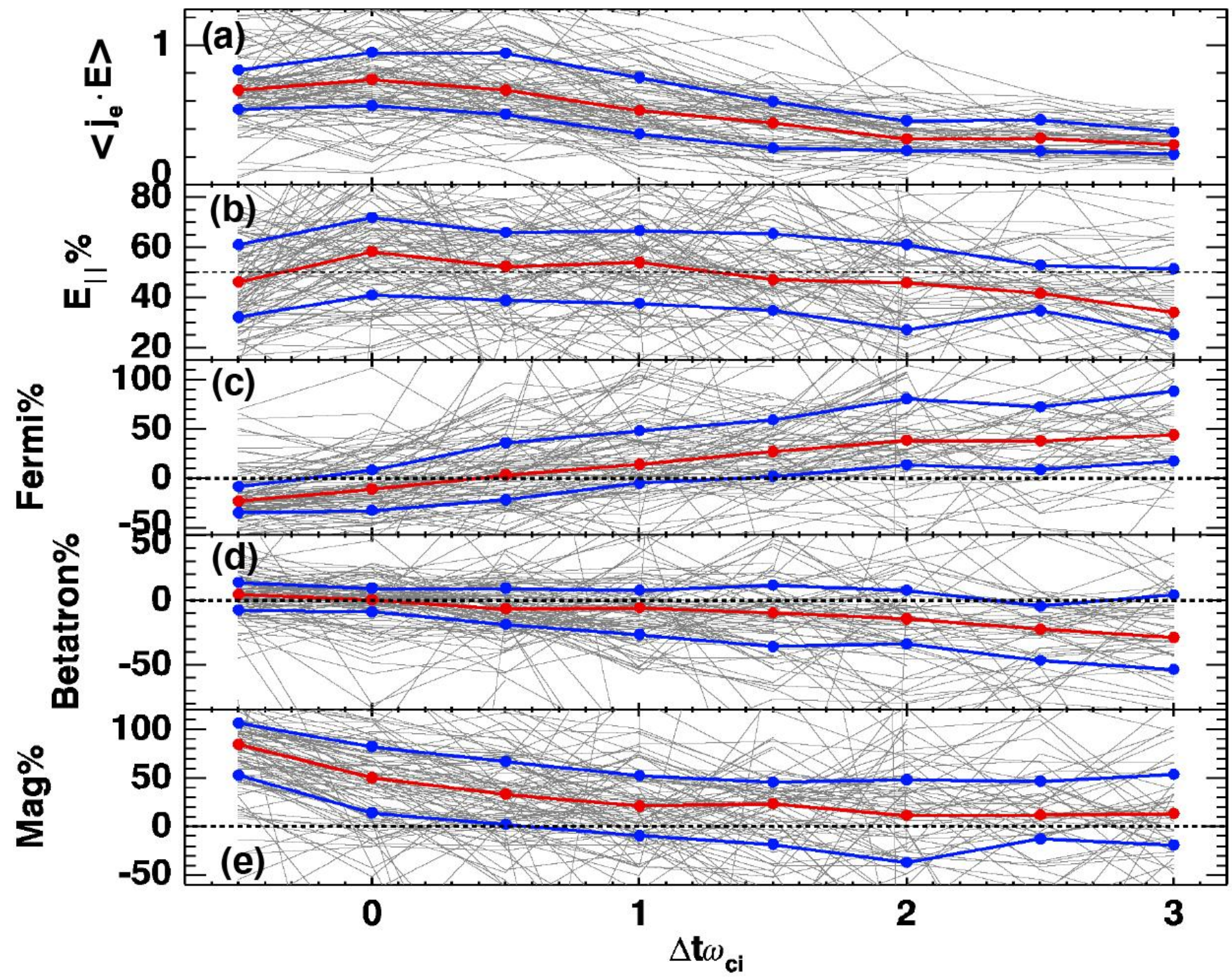

Figure 6. Superposed epoch analysis of $\boldsymbol{j_e} \cdot \boldsymbol{E}$ and its decompositions. The formats are the same with those in Figure 4. (a) Average $\boldsymbol{j_e} \cdot \boldsymbol{E}$ per unit area. (b)-(e) the ratio between each term and total $\boldsymbol{j_e} \cdot \boldsymbol{E}$. At the early time, $E_{\parallel}$ slightly dominates the energization, and the magnetization term dominates the perpendicular energization. The Fermi term exhibits a reversal from negative to positive values and becomes dominant at a couple ω_{ci}^{-1} after reconnection starts.

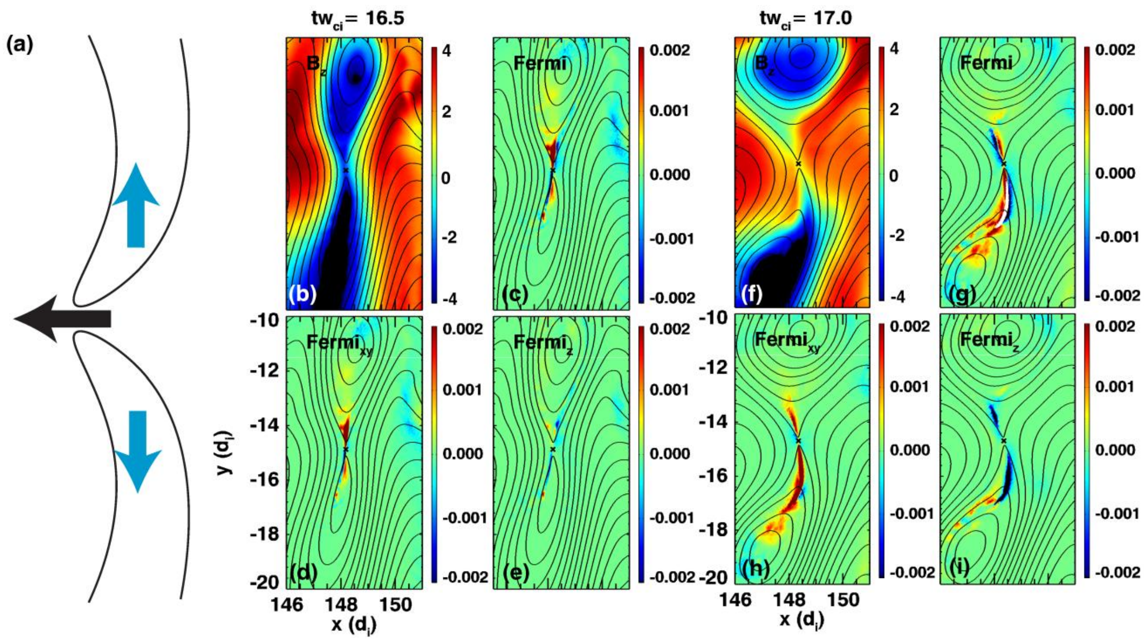

Figure 7. Decomposition of the Fermi term for the example single current sheet. (a) An illustration showing that the flow and curvature are along the same direction for the outflow in the reconnection plane (red), contributing positive Fermi values; the two have opposite signs in the out-of-plane direction due to the Hall effect, which lead to negative values. (b)-(e) are for $t\omega_{ci} = 16.5$ when reconnection starts and the net Fermi contribution is negative. (f)-(i) is for $t\omega_{ci} = 17.0$ with a net positive Fermi contribution. The four panels at each time show B_z, total Fermi term, in-plane Fermi term (Fermi$_{xy}$) and the out-of-plane Fermi term (Fermi$_z$). Overall it shows the competition between the positive in-plane contribution and the negative out-of-plane contribution.

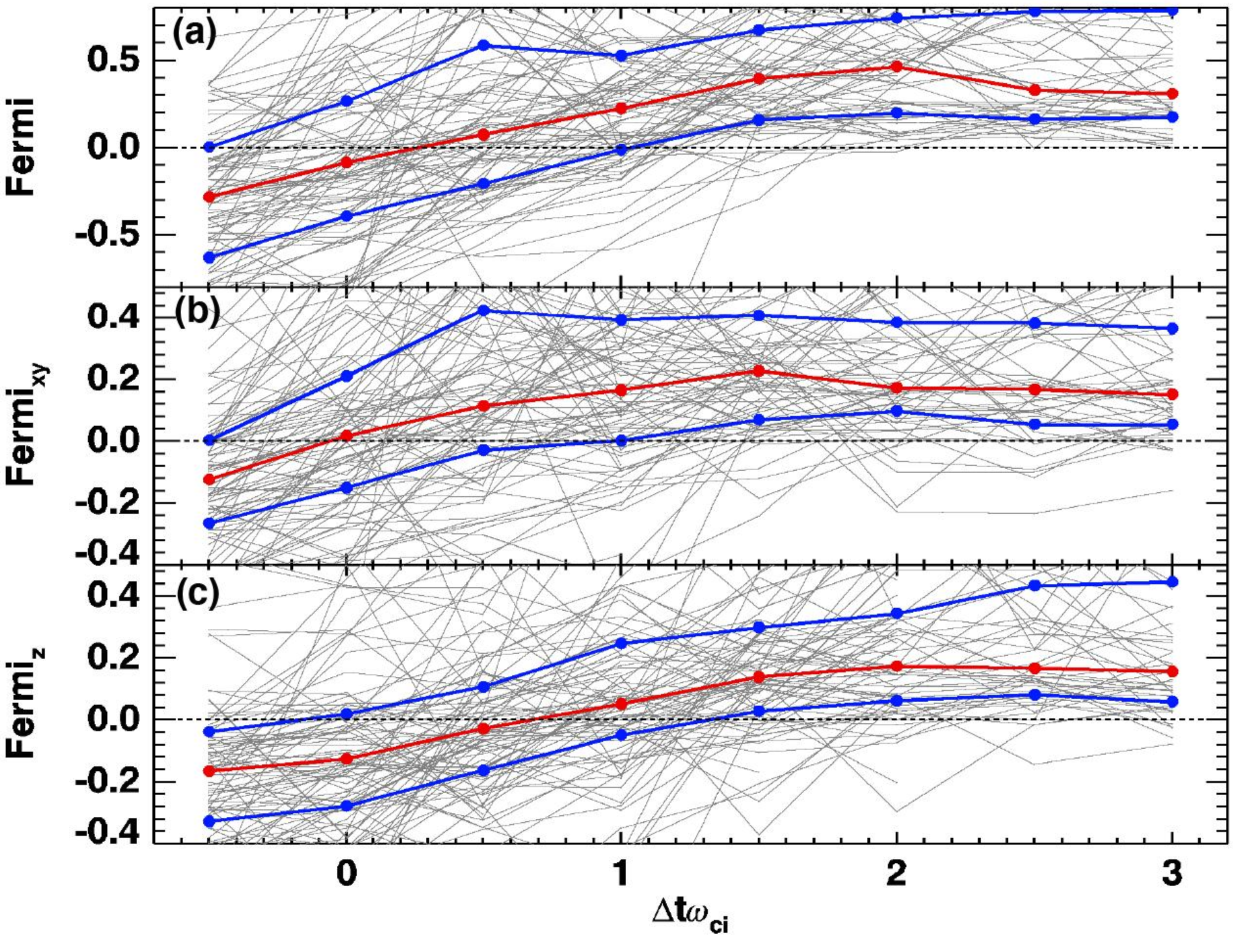

Figure 8. Superposed epoch analysis for Fermi decompositions. The formats are the same with Figure 4. (a) The total Fermi term, (b) in-plane Fermi term (Fermi_{xy}), (c) out-of-plane Fermi term (Fermi_{z}). Fermi_{xy} is mainly positive, consistent with the reconnection outflow feature, while at the early time before reconnection starts, it can has negative values. Fermi_{z} stays at negative values for longer time than Fermi_{z}, associated with the Hall effect, and it can become positive later as the reconnection structure becomes more complicated.

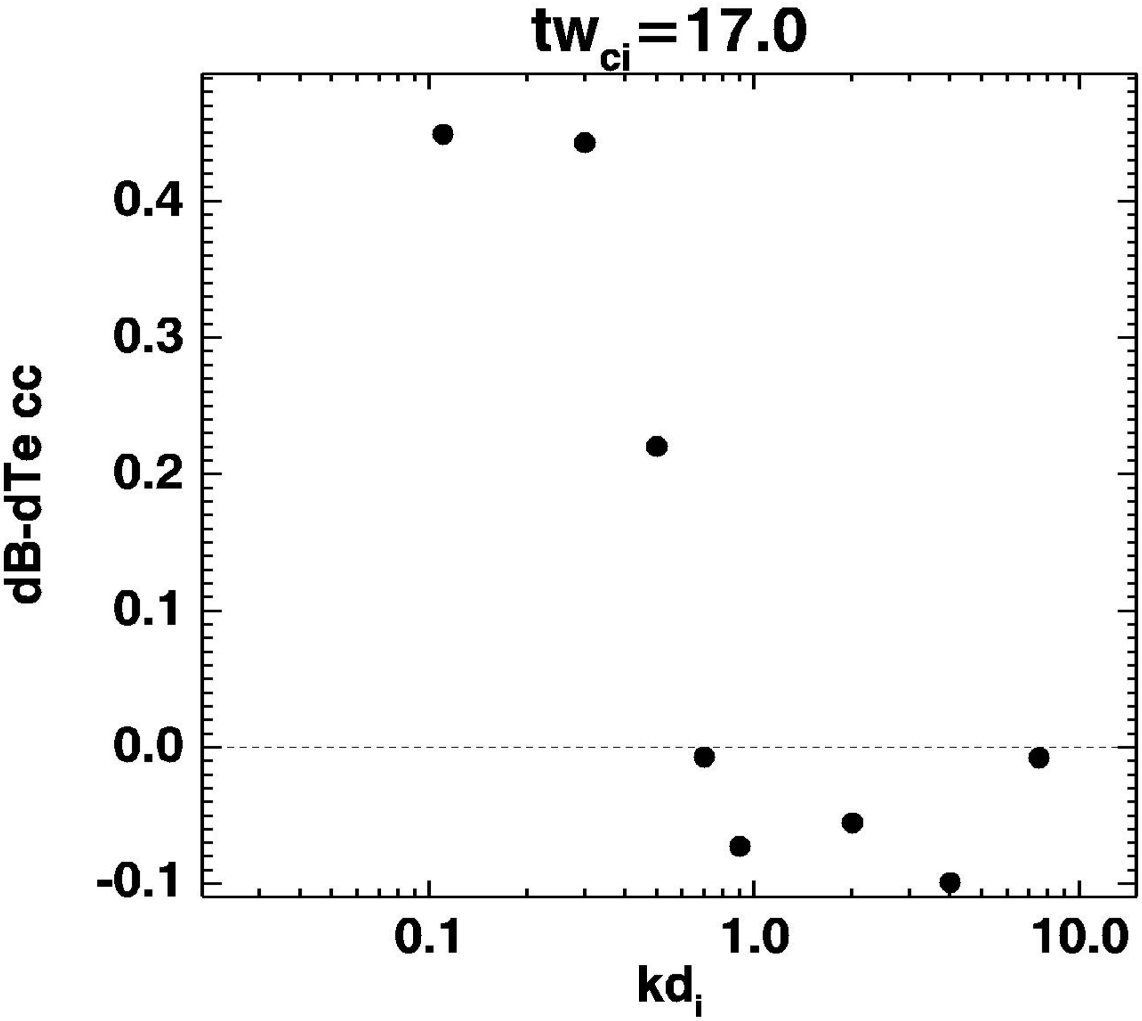

Figure 9. The correlation coefficient between |B| and T_e filtered at different spatial scales. The two quantities exhibit positive correlations at $kd_i \lesssim 0.7$, consistent with the adiabatic heating. Weak negative correlations exist at $kd_i \gtrsim 0.7$, associated with heating contributions by low magnetic field structures like reconnection current sheets.

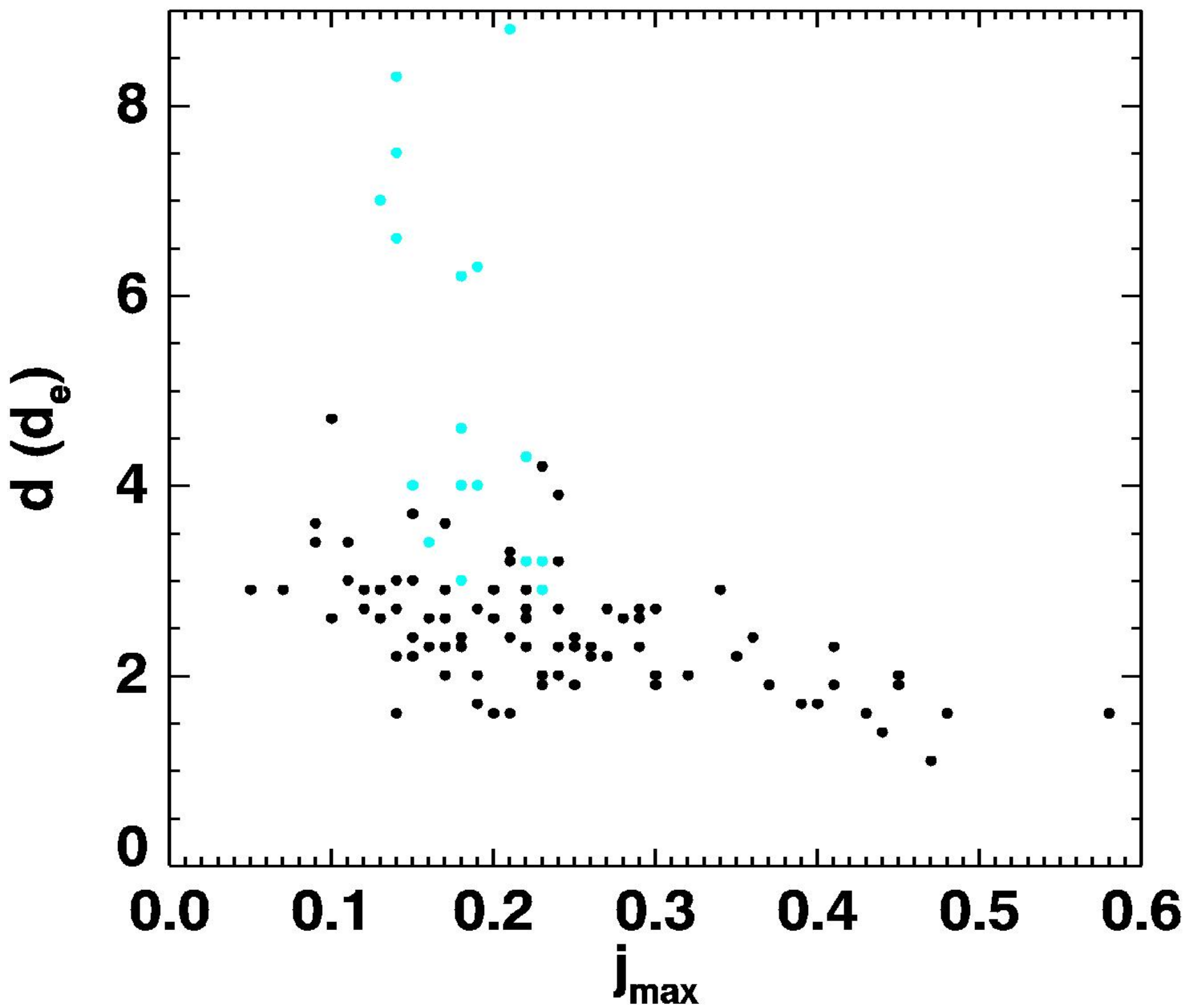

Figure 10. Statistics of the current sheet thickness, represented by the full width at half maximum of $|j_z|$ in a cut along N across the X-line, as a function of the maximum current density. Reconnection current sheets (black) tend to have smaller thicknesses than non-reconnection current sheets (cyan).

Electron heating associated with magnetic reconnection in foreshock waves: particle-in-cell simulation analysis

Shan Wang[1*], and Yan Yang[2]

[1]Institute of Space Physics and Applied Technology, Peking University, Beijing 100871, China

[2]Department of Physics and Astronomy, University of Delaware, Newark, DE 19716, USA

*coralwang90@gmail.com

Key points

- Statistically electrons are heated in reconnection with the temperature increase at 10%~40% of the available magnetic energy for reconnection
- The electron bulk energization is dominant by $E_{||}$ around reconnection onset, and is later dominant by Fermi acceleration
- Driving the current sheet to the d_e-scale thickness is critical for initiating reconnection, and interactions of multiple reconnection sites lead to complicated structures

Abstract

Magnetic reconnection occurs in turbulent plasmas like shock transition regions, while its exact role in energy dissipation therein is not yet clear. We perform a 2D particle-in-cell simulation for foreshock waves and study electron heating associated with reconnection. The probability distribution of T_e exhibits a shift to higher values near reconnection X-lines compared to elsewhere. By examining the T_e evolution using the superposed epoch analysis, we find that T_e is higher in reconnection than in non-reconnecting current sheets, and T_e increases over the ion cyclotron time scale. The heating rate of T_e is 10%-40% $m_i V_A^2$, where V_A is the average ion Alfvén speed in reconnection regions, which demonstrates the importance of reconnection in heating electrons. We further investigate the bulk electron energization mechanisms by decomposing $\boldsymbol{j_e} \cdot \boldsymbol{E}$ under guiding center approximations. Around the reconnection onset, $E_{||}$ dominates the total energization partly contributed by electron holes, and the perpendicular energization is dominant by the magnetization term associated with the gyro-motion in the inhomogeneous fields. The Fermi mechanism contributes negative energization at early time mainly due to the Hall effect, and later the outflow in the reconnection plane contributes more dominant positive values. After a couple of ion cyclotron periods from reconnection onset, the Fermi mechanism dominates the energization. A critical factor for initiating reconnection is to drive current sheets to the d_e-scale thickness. The reconnection structures can be complicated due to flows originated from the ion-scale waves, and interactions between multiple reconnection sites. These features may assist future analysis of observation data.

1. Introduction

Magnetic reconnection is a ubiquitous plasma process that converts energies from electromagnetic fields to particles. Commonly happening in the turbulent environment, such as the Earth's magnetosheath [e.g., Voros et al., 2017; Phan et al., 2018; Starwarz et al., 2022; Wilder et al., 2022] and the shock transition region [e.g., Gingell et al., 2019, 2020; Wang et al., 2019, 2020; Liu et al., 2020], reconnection can potentially contribute to the energy dissipation therein. In observations, the clearest reconnection signature is the outflow jet for electrons [e.g., Phan et al., 2018], sometimes for ions [e.g., Wang et al., 2019], and the inflow and outflow of the magnetic flux [e.g., Qi et al., 2022]. The outflow is also the primary criterion for identifying reconnection events. The effect on electron heating is less clear. Some individual events exhibit T_e enhancements in the reconnection current sheets [e.g., Gingell et al., 2019; Wang et al., 2019; Liu et al., 2020], and some do not [e.g., Phan et al., 2018; Wang et al., 2020]. A statistical examination [Gingell et al., 2020] shows that the electron heating rate ($\Delta T_e/m_i V_A^2$, i.e., the temperature increase from inflow to outflow regions of reconnection with respect to the inflow magnetic energy) can be either positive or negative. The width of the heating rate distribution is much greater than that in typical magnetopause reconnection of 1.7% [Phan et al., 2013], and can exceed 100% in some cases. As discussed in Gingell et al. [2020], electron heating may also occur outside of the reconnection current sheets in the shock transition region, which complicates the observation features. Recent simulation studies have shown that reconnection in turbulence contributes to electron heating: Shay et al. [2018] found that the scaling of ion and electron heating in single reconnection events is applicable to turbulence, while the number of reconnecting X-lines is important in determining the actual heating amount; Bandyopadhyay et al. [2021] demonstrated electron heating in individual reconnection X-line regions diagnosed with the pressure work. Here we use a simulation to study electron heating in reconnection in the shock transition region, aiming to find out explicitly whether reconnection is important for heating electrons in such an environment, to understand the electron energization mechanisms in the framework of guiding center motion, and to advance the understanding of structures and evolution of reconnection in the shock turbulence.

For reconnection in the shock transition region, one pathway of generating reconnection current sheets is through the evolution of foreshock waves, as demonstrated by particle-in-cell (PIC) simulations [Bessho et al., 2020] and inferred from observations [Wang et al., 2020]. In the transition region of quasi-parallel shocks, the presence of counter-streaming ions between the incoming solar wind and the backstreaming population can initiate ion-ion beam instability and generate ULF waves with a wavelength of a few to tens of ion inertia lengths (d_i) [e.g., Eastwood et al., 2005; Wilson III, 2016]. The ULF wave grows into large amplitudes, sometimes generating non-linear structures like Short Large-Amplitude Magnetic Structures (SLAMS) [e.g., Schwartz et al., 1992; Wang et al., 2020; Chen et al., 2021]. The waveform in the ion-scale waves gradually distorts, and secondary instabilities may also be excited, which both lead to thin current sheets that eventually reconnect [Bessho et al., 2020]. In this study, we extract the foreshock environment in the shock to simulate the ion-ion instability and the processes that follow.

2. Simulation

We perform a 2D PIC simulation in the x-y plane using the VPIC code [Bowers, 2008]. The simulation starts from a homogeneous magnetic field $\mathbf{B}_0$ along x. A solar wind ion population moves with a bulk $V_x<0$, a backstreaming ion population moves with $V_x>0$, and electrons are at rest. The density ratio between backstreaming ions and electrons is $n_b/n_0=0.2$, the relative drift between two ion populations is $dV=15\ V_{A0}$, where V_{A0} is the ion Alfvén speed based on B_0 and n_0. The solar wind ion β is 1.0, the temperature ratio between backstreaming ions and solar wind ions is $T_b/T_{SW}=25$, and the temperature ratio between electrons and solar wind ions is $T_e/T_{SW}=2$. The simulation uses periodic boundary conditions along both directions. The system size is $L_x \times L_y=240\ d_i \times 120\ d_i$, the grid size in each dimension is $0.19\ d_e$, the mass ratio is $m_i/m_e=100$, and the electron plasma to cyclotron frequency ratio is $\omega_{pe}/\omega_{ce} = 5$. Unless otherwise noted, the magnetic and electric field are in units of B_0, density is in n_0, velocity is in speed of light (c), and temperature is in m_ec^2.

Under the simulated initial conditions, where n_b/n_0 and dV are the most critical parameters, the linear instability analysis predicts the excitation of the non-resonant mode ion-ion beam instability [e.g., Akimoto et al., 1993] (not shown). The corresponding ULF wave propagates toward -x with a right-hand polarization. The wave does not resonate with backstreaming ions (the reason for the name of 'non-resonant' mode) but cyclotron resonates with solar wind ions. Such simulation setups for 1D runs in the same parameter regime have been used to successfully produce the non-resonant ULF wave and the associated nonlinear solitary structures [Chen et al., 2021; Chen et al., 2022]. Here the simulation is extended to 2D, and it still leads to the non-resonant mode wave in the linear stage as predicted. The simulation represents the foreshock wave environment, and we will investigate its evolution, particularly about electron heating in reconnection born out of the foreshock waves.

3. Electron heating in reconnection current sheets

The simulation develops the non-resonant mode ion-ion instability. The corresponding wave has a wavelength of 6.7 d_i, propagating toward -x with a speed of 2.2 V_{A0} with a right-hand polarization, and the frequency is $\omega = 2.0\omega_{ci}$. At $t\omega_{ci} = 17.0$, the wave magnetic field $dB = \sqrt{B_y^2 + B_z^2}$ grows to the largest spatially averaged value of 2.2 B_0, with a local maximum amplitude of 7.3 B_0. The B_y field is shown in Figure 1a. The B_y stripes are mainly along y and have been broken into segments of current sheets. The overplotted magnetic field lines in the x-y plane (black curves) show the formation of islands that indicate reconnection, and the 'x' symbols mark the X-point locations determined by the saddle points of the vector potential A_z with optimal data smoothing [Haggerty et al., 2017]. T_e exhibits enhancements that tend to be associated with current sheets (Figure 1b).

We examined the evolution of individual reconnection current sheets. An example is shown in Figure 2 (a-e). Around $t\omega_{ci} = 16.0$, magnetic fields in the shown region of a few d_i are compressed to a strength of ~5 B_0 (Figure 2a), which can be considered as a SLAMS. The compressed region is associated with electron heating (Figure 2b). The current sheet in the center is further compressed to the electron scale and reconnection occurs at $t\omega_{ci} = 16.5$ (Figure 2c), where T_e is more significantly enhanced. The current sheet thickness when X-line first appears at $t\omega_{ci} = 16.5$ is 1.6 d_e, based on the full width at half maximum of j_M along N across the X-line (not shown). The LMN coordinate system is determined and illustrated on V_{eL} profiles (Figures 2d-2e): M=z is along the out-of-plane current direction; L is along the maximum variance direction of the x-y plane magnetic fields in a region of 2 d_i×2 d_i surrounding the X-line, and N finishes the right-handed L-M-N coordinate. V_{eL} exhibits a field-aligned shear flow on two sides of the current sheets. The flow shear develops before reconnection starts. It is originally the flow along the ion-scale wave magnetic fields as the wave grows to large amplitudes, and becomes the shear flow as field lines bend to form the current sheet. The shear flow gradually evolves into part of the reconnection outflow jet (Figure 2e). At $t\omega_{ci} = 16.5$, the shear flow is 6.3 $V_{A,asym}$, where $V_{A,asym} = \sqrt{\frac{|B_{L1}B_{L2}|(|B_{L1}|+|B_{L2}|)}{m_i(n_1|B_{L2}|+n_2|B_{L1}|)}}$ is the inflow ion Alfvén speed for asymmetric reconnection, and parameters for calculating the shear flow and $V_{A,asym}$ are taken at inflow regions where $|j_M|$ drops to 1/10 of its maximum. Ions are demagnetized and V_{iL} also exhibits diverging outflows but with a much smaller amplitude than V_{eL} (not shown), indicating that ions are involved in reconnection, but the region is not large enough to fully develop magnetized ion outflow jets. The shear flow is much greater than the critical value of ~2$V_{A,asym}$ (for weak asymmetry as in this current sheet) that was predicted to suppress reconnection [Doss et al., 2015]. We suspect that the incomplete coupling of ions may play a role in allowing for reconnection to happen, since the electron mass or something between ion and electron masses may be more appropriate to characterize the Alfvén speed that sets the shear flow threshold; the strong driving condition in the turbulence may also be helpful for sustaining reconnection. It requires future work to better understand whether and how shear flow effects on reconnection vary under these circumstances.

The turbulent environment generates many reconnection current sheets, and some can be close to and affected by each other. Figure 2f shows an example cluster of current sheets with multiple X-lines. Arrows indicate the inflow and outflow directions at each reconnection site, based on the consistent indicators of the direction of E_z, evolution of the A_z contours, and the direction of electron outflow jets. The islands generated by X-lines No. 1 and No. 2 connect to the inflow region of X-line No. 3, so the reconnection jets around these islands can help drive the inflow of reconnection No. 3. X-line No. 4 is in the exhaust of reconnection No. 3. A band of T_e enhancement spans from X-line No. 3 to the inflow region of reconnection No. 4, indicating the flow of energized particles between reconnection sites, and these particles can thus be energized by multiple reconnection sites. The source of energized particles from reconnection No. 3 also leads to a complicated T_e profile. Along the trajectory marked by the magenta line in Figure 2f, the enhanced T_e band from the different X-line leads to asymmetric inflow T_e conditions for reconnection site No. 4, and T_e in the exhaust is lower than T_e in the inflow. Such an observation feature might be mis-interpreted as low/negative heating rate by reconnection, but the high inflow T_e is actually due to other mechanisms rather than the observed reconnection current sheet.

The importance of reconnection in the statistical sense is evaluated by plotting the probability distribution function (pdf) of T_e (Figure 3). The plot is for $t\omega_{ci} = 18.0$, where the number of X-lines reaches the maximum of 328, while the features are persistent for all time steps with X-lines. Compared to the pdf of all cells (black), the pdf of T_e for cells at 2 $d_e \times$ 2 d_e surrounding X-lines (red) is clearly shifted to higher T_e values. The pdf of T_e surrounding O-lines (defined by extrema of A_z) also exhibits a shift of the peak to higher T_e values than pdf of all cells, but the shift is smaller than that for X-lines; it has a positive skewness with higher pdf than that for all cells at high T_e. The result indicates the statistical importance of electron heating by reconnection.

The T_e evolution of reconnection current sheets is further examined to extract more quantitative results. For the single current sheet in Figure 2 (a-e), we analyze the fixed region shown in the plot with a size of 5 $d_i \times$ 10 d_i. The average T_e over the fixed region at each time step increases over time (Figure 4a, blue), and the heating rate $\Delta T_e/m_i V_A^2$ increases from 7% at $t\omega_{ci} = 16.0$ to 21% at $t\omega_{ci} = 19.5$ (X-line first appears at $t\omega_{ci} = 16.5$). Here ΔT_e is the difference between the spatially averaged T_e and the simulation initial T_{e0}=0.05 (close to the value of the minimum T_e in the region), and V_A is the ion Alfvén speed based on the average n_e and |B| over the region at the instant time. T_e close to the X-line (averaged over 2 d_e × 2 d_e) is separately examined (Figure 4a, orange), which is usually greater than the ion-scale averaged T_e, while it occasionally may exhibit a decrease over time. The rate $\Delta T_e/m_i V_A^2$ close to the X-line is up to 30% (Figure 4b, orange). We note that the calculation of the heating rate has some differences from the typical way applied to reconnection studies [e.g., Phan et al., 2013; Shay et al., 2014], where ΔT_e is the difference between the outflow and inflow, and V_A is based on the density and the reconnecting component of the magnetic field in the inflow region. We applied the same method for some current sheets, where the outflow T_e is taken close to the X-line. The resulting heating rate varies over a larger range than those shown in Figure 4b, even for current sheets with simple structures, indicating more variability of heating in reconnection of such a turbulent environment. The complicated orientations and inhomogeneous inflow conditions lead to additional uncertainties when evaluating the heating rate. Therefore, we choose to use the presented method to avoid ambiguity, and the method is expected to be also applicable to 3D simulations and observations after minor modifications.

A statistical study of T_e evolution is performed using the superposed epoch analysis. We select 59 well isolated reconnection current sheets like that shown in Figure 2 (a-e) and 43 clusters of reconnection current sheets like in Figure 2f, 102 in total. Each single or cluster of current sheets is considered as one event, and we require at least one X-line in the event lasts for longer than 1

ω_{ci}^{-1}. For each event, we analyze a region with a fixed area, typically including a couple of d_i away from the current sheets like those shown in Figure 2. In cases where the X-line has significant displacements over time, the region for the analysis moves to capture the current sheet, while the area remains fixed. Figure 4c shows the superposed epoch analysis of the average T_e over the regions of each event. Each gray curve represents the time evolution of T_e for individual events. Epoch t=0 is defined as the time where X-line first appears, which is typically at $t\omega_{ci} = 16.0{\sim}17.0$. The red curve represents the median value of T_e over different events at each time; blue curves represent the 25% and 75% quartiles. Some reconnection events may not last as long as 3 ω_{ci}^{-1}, and the statistics at each time is only for the available events. In addition, we select 17 non-reconnection current sheets, where the maximum $|j_z|$ is greater than 3 times of standard deviation of $|j_z|$ in the entire simulation domain, but reconnection never occurs to form an X-line. The green curve shows the T_e evolution of these non-reconnection events during $t\omega_{ci} = 15.5{\sim}19.0$. It is clear that T_e of reconnection current sheets is greater than that of non-reconnection current sheets, and also increases over time. Figure 4d shows $\Delta T_e/m_i V_A^2$ that represents the heating rate by reconnection current sheets. Considering the range of 25%-75% quartiles, it increases from ~8% around the reconnection onset to 20%-30% at 3 ω_{ci}^{-1}, where both T_e and $\Delta T_e/m_i V_A^2$ start to approach to saturations. T_e close to the X-line (Figure 4c) exhibits a significant jump as reconnection starts, and statistically remains at steady values in the later time that are greater than the average T_e over a bigger region. The heating rate close to the X-line continues to increase from 10%-20% when reconnection starts to 25%-40% at 3 ω_{ci}^{-1}. The clearer increase of the heating rate than T_e in the later time indicates decrease of V_A and thus the reduction of the electromagnetic energy for reconnection.

The events included in the superposed epoch analysis cover about ¼ of the simulation domain. Later in time, the heated regions further spread as energized particles move around, and the entire simulation domain has a relatively smooth temperature of 0.1 m_ec^2, well represented by the saturation level of reconnection current sheets (Figure 4c).

4. Electron energization

Knowing that reconnection indeed contributes significant electron heating in the foreshock wave environment, we next investigate the electron energization mechanisms. First we will analyze the electron energy equations to see that $\boldsymbol{j_e} \cdot \boldsymbol{E}$ measures the electron energization, and the electron energization is dominant by the electron thermal energy gain. By taking the second-order moments of the Vlasov equation, we can obtain the energy equation of electrons, which can be further decomposed into the flow energy equation:

$$\frac{\partial u_{bulk,e}}{\partial t} + \nabla \cdot \boldsymbol{K_e} = \boldsymbol{j_e} \cdot \boldsymbol{E} - \boldsymbol{V_e} \cdot (\boldsymbol{\nabla} \cdot \boldsymbol{P_e}) \quad (1)$$

and thermal energy equation [e.g., Lu et al., 2018; Lapenta et al., 2020]:

$$\frac{\partial u_{th,e}}{\partial t} + \nabla \cdot \boldsymbol{H_e} + \boldsymbol{\nabla} \cdot \boldsymbol{q_e} = \boldsymbol{V_e} \cdot (\boldsymbol{\nabla} \cdot \boldsymbol{P_e}) \quad (2)$$

where $u_{bulk,e} = \frac{1}{2} m_e n_e V_e^2$ is the electron bulk flow energy density, $\boldsymbol{K_e} = \frac{1}{2} m_e n_e V_e^2 \boldsymbol{V_e}$ is the bulk flow energy flux, $\boldsymbol{j_e} =- n_e \boldsymbol{V_e}$ is the electron current density, $u_{th,e} = \frac{3}{2} n_e T_e$ is the thermal energy density, $\boldsymbol{H_e} = \boldsymbol{P_e} \cdot \boldsymbol{V_e} + u_{th,e} \boldsymbol{V_e}$ is the enthalpy flux, and $\boldsymbol{q_e} = m_e \int f |\boldsymbol{v} - \boldsymbol{V_e}|^2 (\boldsymbol{v} - \boldsymbol{V_e}) d^3 v$ is the heat flux. One way to understand equations (1) and (2) is to view the left-hand sides as the gain of flow or thermal energies, which includes both the temporal evolution of $u_{bulk,e}$ and $u_{th,e}$ in the specific region and the net energy flux across the region. It is a picture that typically applies to reconnection [e.g., Eastwood et al., 2013; Shay et al., 2014; Yamada et al., 2016;

Wang et al., 2018] and shocks [e.g., Schwartz et al., 1987; Schwartz et al., 2022], and usually the explicit time dependence can be further neglected in these situations. $\boldsymbol{j_e} \cdot \boldsymbol{E}$ represents the energy conversion from electromagnetic fields to electrons, and $\boldsymbol{V_e} \cdot (\boldsymbol{\nabla} \cdot \boldsymbol{P_e})$ alters the partition between flow and thermal energies. From the electron momentum equation, the electric field can be expressed as:

$$\boldsymbol{E} = - \boldsymbol{V_e} \times \boldsymbol{B} - \frac{1}{n_e e} \boldsymbol{\nabla} \cdot \boldsymbol{P_e} - \frac{m_e}{n_e e} \frac{d\boldsymbol{V_e}}{dt} \quad (3)$$

For electrons, the inertial term (last term in eq.(3)) is usually negligible due to its small mass (confirmed with our simulation data), so the non-ideal electric field in the electron bulk frame $\boldsymbol{E}^{'} = \boldsymbol{E} + \boldsymbol{V_e} \times \boldsymbol{B}$ is dominated by $-\frac{1}{n_e e} \boldsymbol{\nabla} \cdot \boldsymbol{P_e}$. The energy conversion satisfies $\boldsymbol{j_e} \cdot \boldsymbol{E} = \boldsymbol{j_e} \cdot \boldsymbol{E}'$, while $\boldsymbol{V_e} \cdot (\boldsymbol{\nabla} \cdot \boldsymbol{P_e}) = \boldsymbol{j_e} \cdot (-\frac{1}{n_e e} \boldsymbol{\nabla} \cdot \boldsymbol{P_e})$. Thus, the two terms on the right-hand side of the flow energy equation (1) almost cancel with each other, indicating that the electron energization is dominated by the thermal energy gain. In observations of reconnection in the shock transition region, despite that the electron outflow jet is usually the clearest feature, the thermal energy gain should be the dominant form based on the above theoretical derivations.

More insights about the energization mechanisms can be obtained by decomposing $\boldsymbol{j_e} \cdot \boldsymbol{E}$:

$$\boldsymbol{j_e} \cdot \boldsymbol{E} = \boldsymbol{j}_{\boldsymbol{e}||} \cdot \boldsymbol{E}_{||} + \boldsymbol{j}_{\boldsymbol{e}\perp} \cdot \boldsymbol{E}_{\perp} \quad (3)$$

When electrons are mostly magnetized and the guiding center approximation is valid, the electron perpendicular drift can be decomposed as [e.g., Parker et al., 1957; Li et al., 2015]

$$\boldsymbol{j}_{\boldsymbol{e}\perp} = - ne \frac{\boldsymbol{E} \times \boldsymbol{B}}{B^2} + P_{e||} \frac{(\boldsymbol{B} \times \boldsymbol{\kappa})}{\boldsymbol{B^2}} + \frac{P_{e\perp}}{\boldsymbol{B^3}} (\boldsymbol{B} \times \boldsymbol{\nabla B}) - \left[\boldsymbol{\nabla} \times \frac{P_{e\perp} \boldsymbol{B}}{\boldsymbol{B^2}}\right]_{\perp} \quad (4)$$

representing the $\boldsymbol{E}\times\boldsymbol{B}$ drift, curvature drift, gradient-B drift, and magnetization drift, respectively, where the polarization drift has been neglected. Plugging it into equation (3), we get:

$$\boldsymbol{j_e}\cdot\boldsymbol{E}=\boldsymbol{j}_{e||}\cdot\boldsymbol{E}_{||}+P_{e||}\frac{(\boldsymbol{B}\times\boldsymbol{\kappa})\cdot\boldsymbol{E}}{\boldsymbol{B}^2}+\frac{P_{e\perp}}{\boldsymbol{B}^3}(\boldsymbol{B}\times\boldsymbol{\nabla B})\cdot\boldsymbol{E}-\left[\boldsymbol{\nabla}\times\frac{P_{e\perp}\boldsymbol{B}}{\boldsymbol{B}^2}\right]_{\perp}\cdot\boldsymbol{E}\ (5)$$

The second term $P_{e||}\frac{(\boldsymbol{B}\times\boldsymbol{\kappa})\cdot\boldsymbol{E}}{\boldsymbol{B}^2}$ represents Fermi acceleration. The third term $\frac{P_{e\perp}}{\boldsymbol{B}^3}(\boldsymbol{B}\times\boldsymbol{\nabla B})\cdot\boldsymbol{E}$ represents Betatron acceleration. The last term is for the magnetization current $-\left[\boldsymbol{\nabla}\times\frac{P_{e\perp}\boldsymbol{B}}{\boldsymbol{B}^2}\right]_{\perp}$ that is associated with the collective gyro-motion in regions with inhomogeneous magnetic fields and pressure. The magnetization current can be further expressed as $-\frac{\nabla_{\perp}P_{e\perp}\times\boldsymbol{B}}{B^2}-P_{e\perp}\frac{(\boldsymbol{B}\times\boldsymbol{\kappa})}{\boldsymbol{B}^2}-\frac{P_{e\perp}}{\boldsymbol{B}^3}(\boldsymbol{B}\times\boldsymbol{\nabla B})$, where the first term is the diamagnetic current, the second term resembles the curvature drift by replacing $P_{e||}$ with $-P_{e\perp}$, and the third term cancels the gradient-B drift. Note that with some re-arrangements of the terms, we get $\boldsymbol{j}_{e\perp}=-ne\frac{\boldsymbol{E}\times\boldsymbol{B}}{B^2}-\frac{\nabla_{\perp}P_{e\perp}\times\boldsymbol{B}}{B^2}+(P_{e||}-P_{e\perp})\frac{(\boldsymbol{B}\times\boldsymbol{\kappa})}{\boldsymbol{B}^2}$ [e.g., Zelenyi et al., 2004; Hwang et al., 2021], so the net drifts that can contribute to $\boldsymbol{j_e}\cdot\boldsymbol{E}$ (i.e., except for the $\boldsymbol{E}\times\boldsymbol{B}$ drift) are the diamagnetic drift and the curvature-related drift if an anisotropy exists, while the gradient-B drift of particles (i.e., Betatron mechanism) does not have a net contribution to the fluid. The way of decomposition in equation (4) is still valuable, since it distinguishes the drifts related to the guiding center motion (curvature, gradient-B drifts) and those related to gyrations around the magnetic field (magnetization drift). It also helps understand how representative particles with the thermal energy can be energized through the Fermi and Betatron mechanisms.

The profiles of individual terms in equation (5) for the example single current sheet (Figure 2 top) when X-line first appears are shown in Figure 5 (top). Such decomposition is based on the guiding center approximation, so it only applies to regions where the local $K = \sqrt{(R_C/r_g)} > 1$, where R_C is the magnetic curvature radius, and r_g is the electron thermal gyro-radius. At the shown time, the guide field for reconnection at the X-line is about 60% of the reconnecting magnetic field in the inflow region, and the entire presented region satisfies $K > 1$. Strong $\boldsymbol{j}_{\boldsymbol{e}||} \cdot \boldsymbol{E}_{||}$ shows up (Figure 5a), with predominantly positive values in the X-line vicinity and bipolar structures along the separatrices, which are consistent with electron holes and lead to segments of T_e enhancements (Figure 2c, enhancements confirmed to be in the $T_{e||}$ component). $\boldsymbol{j}_{\boldsymbol{e}\perp} \cdot \boldsymbol{E}_{\perp}$ is weaker than $\boldsymbol{j}_{\boldsymbol{e}||} \cdot \boldsymbol{E}_{||}$ at the X-line, but has strong enhancements in the reconnection exhaust only a few d_e downstream of the X-line. Decomposing $\boldsymbol{j}_{\boldsymbol{e}\perp} \cdot \boldsymbol{E}_{\perp}$, the strongest enhancement is in the Fermi term in the reconnection exhaust, while some negative values appear; the Betatron term is much weaker, with some localized enhancements downstream of the region with strong Fermi contributions; the magnetization term has moderate enhancements throughout the region, including positive contributions around the X-line.

To evaluate the net contributions of different mechanisms, we examine the integrated $\boldsymbol{j}_{\boldsymbol{e}} \cdot \boldsymbol{E}$ over the region at different time steps. The total $\boldsymbol{j}_{\boldsymbol{e}} \cdot \boldsymbol{E}$ (Figure 5f) is strongest at the start of reconnection ($t\omega_{ci} = 16.5$) and decreases at later time. $\boldsymbol{j}_{\boldsymbol{e}||} \cdot \boldsymbol{E}_{||}$ dominates before and near the reconnection onset ($t\omega_{ci} = 16.0 - 16.5$), $\boldsymbol{j}_{\boldsymbol{e}\perp} \cdot \boldsymbol{E}_{\perp}$ peaks and dominates at $t\omega_{ci} = 17.0$. The decomposition of $\boldsymbol{j}_{\boldsymbol{e}\perp} \cdot \boldsymbol{E}_{\perp}$ is shown in Figure 5g, where the 'demagnetized' term (cyan) represents $\boldsymbol{j}_{\boldsymbol{e}\perp} \cdot \boldsymbol{E}_{\perp}$ in regions with $K < 1$, and other terms are integrated over regions with $K > 1$. The demagnetized term turns out to have a much smaller amplitude than other terms for all the events. The sum of four terms (green) overall agrees with $\boldsymbol{j}_{\boldsymbol{e}\perp} \cdot \boldsymbol{E}_{\perp}$ (blue in Figure 5f), and the difference is mainly attributed to numerical uncertainties, with minor contributions by the imperfect assumptions like gyrotropic pressure tensors. At the early time near the reconnection onset, the net Fermi contribution is negative, and the magnetization term contributes most positive values. Later the Fermi term becomes the dominant mechanism to contribute positive energization. The Betatron term contributes small positive values in most of the interval.

A superposed epoch analysis is performed to examine the energization mechanisms for the 102 events, and the trend is mostly consistent with the example shown in Figure 5. $<\boldsymbol{j_e}\cdot\boldsymbol{E}>$ shown in Figure 6a is the average value per unit area, so that results in different events can be compared. The following panels show the percentage of each term with respect to $<\boldsymbol{j_e}\cdot\boldsymbol{E}>$. $<\boldsymbol{j_e}\cdot\boldsymbol{E}>$ tends to be the strongest near the start of the reconnection, and the values before t=0 is already comparable to those at t=0. Figure 6b-6e show the percentage contributions of different terms with respect to $<\boldsymbol{j_e}\cdot\boldsymbol{E}>$. The contribution by $E_{\parallel}$ (Figure 6b) has a slight decreasing trend over time, where the median value is above 50% at the early time and below 50% later. For the decomposition of $\boldsymbol{j}_{\boldsymbol{e}\perp}\cdot\boldsymbol{E}_{\perp}$, at the later time, the relative importance is consistent with the laminar reconnection studies [e.g., Dahlin et al., 2014, 2015, 2016; Li et al., 2015, 2017]: the Fermi term (Figure 6c) dominates the positive contribution, and the Betatron term (Figure 6d) is negative. The features at the earlier time are different, where the Fermi term is negative, the median value of the Betatron term can be slightly positive before reconnection starts, and the magnetization term (Figure 6e) dominates the positive contribution. We may visualize that as the current sheet thins down and reconnection is initiated, it creates a highly inhomogeneous environment to weakly 'demagnetize' electrons, though the gradient scales are not large enough to fully demagnetize electrons and invalidate the guiding center approximation. The collective gyrations of particles contribute the net current and lead to energizations, manifested as the contribution by the magnetization term.

We look into more details about how the Fermi term appears to be negative values. Mathematically, the Fermi term $P_{e||}\frac{(\boldsymbol{B}\times\boldsymbol{\kappa})\cdot\boldsymbol{E}}{\boldsymbol{B}^2}$ can be re-arranged into $P_{e||}(\boldsymbol{V}_{\boldsymbol{E}\times\boldsymbol{B}}\cdot\boldsymbol{\kappa})$. Therefore, in the reconnection exhaust where both the magnetic curvature and the $\boldsymbol{E}\times\boldsymbol{B}$ outflow velocity point away from the X-line in the reconnection (x-y) plane, the Fermi term is expected to be positive. However, in the ion diffusion region (or electron-only reconnection) where ions and electrons are decoupled, Hall fields develop, where electrons that are roughly frozen-in drag magnetic field lines toward the out-of-plane direction to form the quadrupolar Hall magnetic field [e.g., Mandt et al., 1994]. As illustrated in Figure 7a, the out-of-plane component of the magnetic curvature is opposite to the $\boldsymbol{E}\times\boldsymbol{B}$ drift, resulting in negative values of the Fermi term. Figure 7 shows the decomposition of the Fermi term for the example single reconnection current sheet, where Figures 7b-7e are for $t\omega_{ci}=16.5$ when the net Fermi term is negative, and Figures 7f-7i are for $t\omega_{ci}=17.0$ when the net Fermi term is positive (Figure 5g). At $t\omega_{ci}=16.5$, the guide field B_z in the current layer is negative (Figure 7b). The Fermi term (Figure 7c) is decomposed into the in-plane $Fermi_{xy}$ (Figure 7d) and out-of-plane $Fermi_z$ (Figure 7e) components ($Fermi=Fermi_{xy}+Fermi_z$). $Fermi_{xy}$ exhibits strong positive values in the exhaust as expected, and some negative values appear in the inflow region and some regions further away from the X-line. $Fermi_z$ is mostly negative, consistent with the Hall pattern. At $t\omega_{ci}=17.0$, B_z becomes positive in the current sheet, and the quadrupolar Hall feature becomes clearer (Figure 7f). The positive values in $Fermi_{xy}$ (Figure 7g) extend to further distances from the X-line as the exhaust expands, while Fermi_z (Figure 7h) exhibits strong negative values around the B_z reversal regions.

The superposed epoch analysis of the Fermi term (per unit area) for all selected reconnection current sheets is presented in Figure 8. The net Fermi term has the median value changing from negative to positive values over time (Figure 8a). Fermi_{xy} is negative before reconnection starts and the median value crosses zero at t=0 (Figure 8b). Fermi_z remains at negative values for longer time up to $\Delta t\omega_{ci}{\sim}1$ (Figure 8c). It also reverses to positive values later, and the examinations of individual events reveal that the positive Fermi_z is associated with complicated structures far away from the X-line, irrelevant to the Hall structures.

The analysis suggests a process that around the onset of reconnection, Fermi contributes negative values associated with the electron dragging of field lines, which occurs in the out-of-plane directions due to the Hall effect, as well as in the in-plane components such as in the inflow region. As reconnection develops and the exhaust region expands, the aligned outflow and magnetic curvature in the reconnection plane dominates, leading to positive Fermi contributions.

5. Discussions

The investigations above have demonstrated the importance of magnetic reconnection on electron heating in the foreshock environment, and have revealed the bulk electron energization mechanisms. Through the analysis, we can try to build a picture of the evolution of electron energization. Figure 9 shows the correlation coefficient between filtered fields of the magnetic field strength (dB) and electron temperature (dT_e) at different spatial scales. The results at $t\omega_{ci} =$

17.0 are shown, when an increasing number of X-lines start to appear, and the features are consistent over a few ω_{ci}^{-1}. At large scales of $kd_i \lesssim 0.7$, dB and dT_e exhibit positive correlations with coefficients of ~0.4 (the coefficient at earlier time can be higher up to ~0.8), consistent with adiabatic heating where T_e increases as the magnetic field compresses. At small scales of $kd_i \gtrsim 0.7$, dB and dT_e no longer have good positive correlations, and the coefficient is slightly negative. It reflects that in sub-ion scale structures, electrons tend to be heated in low-field regions such as the reconnection current sheets. Such a feature of electron heating at large and small scales summarizes a consistent picture with the examples we examined (e.g., Figure 2a-2c).

Since we have found that the reconnection current sheets produce more electron heating than non-reconnection current sheets, what is the difference between the two? By examining individual cases, we found that a main difference seems to be the current sheet thickness. We selected 93 reconnection current sheets to calculate their smallest thicknesses, which include the single X-line events used in the above statistics and additional current sheets that are well isolated from others when their thicknesses reach the minimum. The thickness is determined as the full width half maximum of $|j_z|$ in the cut along N across the X-line. The thickness is plotted as a function of the maximum $|j_z|$ (j_{max}) in Figure 10, which lies in the range of 1~5 d_e for reconnection current sheets (black) with a median value of 2.4 d_e. The cyan dots show the thicknesses for 17 non-reconnection current sheets, which is overall greater than those of reconnection current sheets, with a median value of 4.3 d_e. Some non-reconnection current sheets have the thickness reaching the group of reconnection current sheets around 3 d_e; however, we find that they stay at such thin scales only briefly at one time step, while the reconnection current sheets hold the small thickness for longer time. The quantitative result demonstrates the difference in thickness between reconnection and non-reconnection current sheets. It suggests that driving the current sheet to a thin scale for sufficient time is a necessary condition for initiating reconnection, and it seems to be also a sufficient condition in the presented simulation.

6. Conclusions

We have investigated electron heating associated with magnetic reconnection in foreshock waves using a 2D PIC simulation that starts from the ion-ion beam instability. Reconnection develops as the ion-scale waveform distorts to form electron-scale current sheets. We obtain main conclusions regarding the electron heating and energization mechanisms:

(1) T_e is statistically higher close to the reconnection X-line than elsewhere, directly demonstrating the importance of reconnection in heating electrons in such an environment. The statistical analysis of the T_e evolution in individual current sheets shows that T_e in reconnection current sheets is greater than that in non-reconnection current sheets and increases over time for the time scale of a couple ω_{ci}^{-1}. Using $\Delta T_e/(m_i V_{Ai}^2)$ to represent the heating rate, where the parameters are based on the values averaged over a few d_i that covers the whole current sheet, it is about 20%-30% at the near-saturation level. The heating rate at the X-line is 10%-20% at the start of reconnection and increases to 25%-40% at saturation.

(2) The bulk electron energization by reconnection is analyzed by decomposing $\boldsymbol{j_e} \cdot \boldsymbol{E}$ with the guiding center approximation. $E_{||}$ statistically contributes more than 50% of the energization around the onset of reconnection and drops to lower than 50% later, and it is in the form of both reconnection electric field near the X-line and intense bipolar electron holes that usually develop

before reconnection starts. For $\boldsymbol{E}_{\perp}$ contributions, the energization at a couple ω_{ci}^{-1} after reconnection onset is dominant by the Fermi mechanism. At earlier time close to the reconnection onset, the perpendicular energization is dominant by the magnetization term associated with the gyro-motion in the inhomogeneous fields. Meanwhile, the Fermi term first has a net negative contribution and a positive contribution later. A primary contribution to the negative Fermi values is the Hall effect where electrons drag field lines in the out-of-plane direction to form the Hall magnetic field. As reconnection evolves and expands, the positive Fermi terms in the reconnection plane associated with the outflow gradually dominates over the negative Hall contribution.

We note that although the electron energization is through $\boldsymbol{j_e} \cdot \boldsymbol{E}$ and the energization mostly goes to the thermal energy gain, the enhancements of $\boldsymbol{j_e} \cdot \boldsymbol{E}$ and T_e are not correlated in the point-wise sense. The thermal energy gain consists of a more complicated definition of $\frac{\partial u_{th,e}}{\partial t} + \nabla \cdot \boldsymbol{H_e} + \boldsymbol{\nabla} \cdot \boldsymbol{q_e} > 0$. In addition to the T_e enhancement, the compression associated with n and V_e enhancements and the temporal variations (demonstrated to be non-negligible in Figure 4) can also contribute to balance $\boldsymbol{j_e} \cdot \boldsymbol{E}$. That's why we examine $\boldsymbol{j_e} \cdot \boldsymbol{E}$ and T_e separately, and it is reasonable to see lack of simultaneous enhancements of the two during in situ observations.

The characteristics of the reconnection current sheets in the simulation help us understand the features that may be difficult to interpret in observations. One interesting feature common to the current sheets in this simulation is that electrons exhibit shear flows along L, which originates from the flow along the ion-scale wave field and later evolves into part of the reconnection outflow jet (e.g., Figure 2e). The shear flow is sizable: for the reconnection current sheets we examine, the median value of shear flow amplitude at the minimum current sheet thickness is 5.5 $V_{A,asym}$. In addition, in such a turbulent environment, reconnection current sheets develop as clusters. The outflow regions of some current sheets can be the inflow regions of others, and particles can get continuous energization by moving through multiple reconnection sites. It leads to complicated current sheet structures and complicated profiles of quantities like V_e and T_e, which cannot be understood as the result of a single reconnection event. At least based on the result of the presented simulation, reconnection is likely to occur once the current sheet can be driven to small thicknesses. It reminds us that when analyzing observation data, current sheets that have structures inconsistent with the most standard reconnection may still be reconnecting or will reconnect later, and the interactions between multiple current sheets likely affect the structures. The heating and energization in reconnection in the shock transition region like the foreshock waves need further investigations in observations, which can be compared with the simulation results and will probably reveal more interesting facts beyond those in 2D simulations.

Acknowledgments

The simulation data presented in the paper are available at https://zenodo.org/record/7178188#.ZFW8KnZBy5c

References

Akimoto, K., Winske, D., Gary, S. P., & Thomsen, M. F. (1993). Nonlinear evolution of electromagnetic ion beam instabilities. Journal of Geophysical Research, 98(A2), 1419 – 1433. https://doi.org/10.1029/92JA02345

Bandyopadhyay, R., Chasapis, A., Matthaeus, W., et al. (2021), Energy dissipation in turbulent reconnection, Phys. Plasmas, 28, 112305, doi: 10.1063/5.0071015

Bowers, K. J., Albright, B. J., Bergen, B., Yin, L., Barker, K. J., and Kerbyson, D. J., "0.374 Pflop/s trillion-particle kinetic modeling of laser plasma interaction on roadrunner," in Proceedings of the 2008 ACM/IEEE Conference on Supercomputing, SC'08 (IEEE Press, Piscataway, NJ, 2008), pp. 63:1–63:11.

Chen, L. J., Wang, S., Ng, J., Bessho, N., Tang, J. M., Fung, S. F., et al. (2021). Solitary magnetic structures at quasi-parallel collisionless shocks: Formation. Geophysical Research Letters, 48, e2020GL090800. https://doi.org/10.1029/2020GL090800

Chen, L.-J., Halekas, J., Wang, S., DiBraccio, G. A., Romanelli, N., Ng, J., et al. (2022). Solitary magnetic structures developed from gyro-resonance with solar wind ions at Mars and Earth. Geophysical Research Letters, 49, e2021GL097600. https://doi.org/10.1029/2021GL097600

Dahlin, J. T., J. F. Drake, and M. Swisdak (2014), The mechanisms of electron heating and acceleration during magnetic reconnection Phys. Plasmas 21, 092304, doi: 10.1063/1.4894484

Dahlin, J. F. Drake, and M. Swisdak (2015), Electron acceleration in three-dimensional magnetic reconnection with a guide field, Phys. Plasmas 22, 100704, doi: 10.1063/1.4933212

Dahlin, J. F. Drake, and M. Swisdak (2016), Parallel electric fields are inefficient drivers of energetic electrons in magnetic reconnection, Phys. Plasmas, 23, 120704, doi: 10.1063/1.4972082

Doss, C. E., C. M. Komar, P. A. Cassak, F. D. Wilder, S. Eriksson, and J. F. Drake (2015), Asymmetric magnetic reconnection with a flow shear and applications to the magnetopause, J. Geophys. Res. Space Physics, 120, 7748–7763, doi:10.1002/2015JA021489.

Eastwood, J. P., E. A. Lucek, C. Mazelle, K. Meziane, Y. Narita, J. Pickett, and R. Treumann (2005), The foreshock, Space Sci. Rev., 118, 41–94.

Eastwood, J. P., Phan, T. D., Drake, J. F., Shay, M. A., Borg, A. L., Lavraud, B., & Taylor, M. G. G. T. (2013). Energy partition in magnetic reconnection in Earth's magnetotail. Physical Review Letters, 110(22), 225001. https://doi.org/10.1103/PhysRevLett.110.225001

Gingell, I., Schwartz, S. J., Eastwood, J. P., Burch, J. L., Ergun, R. E., Fuselier, S., et al. (2019). Observations of magnetic reconnection in the transition region of quasi-parallel shocks. Geophysical Research Letters, 46, 1177–1184. https://doi.org/10.1029/2018GL081804

Gingell I., Schwartz, S. T., Eastwood, J. P., Stawarz, J. E., Burch, J. L., Ergun, R. E., et al. (2020). Statistics of reconnecting current sheets in the transition region of earth's bow shock. Journal of Geophysical Research: Space Physics, 125, e2019JA027119. https://doi.org/10.1029/2019JA027119

Haggerty,C. C., T. N. Parashar, W. H. Matthaeus, M. A. Shay, Y. Yang, M. Wan, P. Wu, and S. Servidio, "Exploring the statistics of magnetic reconnection x-points in kinetic particle-in-cell turbulence," Phys. Plasmas 24, 102308, https://doi.org/10.1063/1.5001722

Hwang K-J, Dokgo K, Choi E, Burch JL, Sibeck DG, Giles BL, Norgren C, Nakamura TKM, Graham DB, Khotyaintsev Y, Shi QQ, Gershman DJ, Pollock CJ, Ergun RE, Torbert RB, Russell CT and Strangeway RJ (2021) Bifurcated Current Sheet Observed on the Boundary of Kelvin-Helmholtz Vortices. Front. Astron. Space Sci. 8:782924. doi: 10.3389/fspas.2021.782924

Li, X., F. Guo, H. Li, and G. Li (2015), NONTHERMALLY DOMINATED ELECTRON ACCELERATION DURING MAGNETIC RECONNECTION IN A LOW-β PLASMA Astrophys. J. Lett. 811, L24, doi:10.1088/2041-8205/811/2/L24

Li, Xiaocan, Fan Guo, Hui Li, and Gang Li (2017), Particle Acceleration during Magnetic Reconnection in a Low-beta Plasma, The Astrophys. J., 843:21, https://doi.org/10.3847/1538-4357/aa745e

Liu, T. Z., Lu, S., Turner, D. L., Gingell, I., Angelopoulos, V., Zhang, H., et al. (2020). Magnetospheric Multiscale (MMS) observations of magnetic reconnection in foreshock transients. Journal of Geophysical Research: Space Physics, 125, e2020JA027822. https://doi.org/10.1029/2020JA027822

Mandt, M. E., Denton, R. E., & Drake, J. F. (1994). Transition to whistler mediated magnetic reconnection. Geophysical Research Letters, 21(1), 73–76. https://doi.org/10.1029/93gl03382

Parker, E. N. (1957), Newtonian Development of the Dynamical Properties of Ionized Gases of Low Density, Phys. Rev. Lett., 107, 924

Phan, T. D., M. A. Shay, J. T. Gosling, M. Fujimoto, J. F. Drake, G. Paschmann, M. Oieroset, J. P. Eastwood, and V. Angelopoulos (2013), Electron bulk heating in magnetic reconnection at Earth's magnetopause: Dependence on the inflow Alfvén speed and magnetic shear, Geophys. Res. Lett., 40, doi:10.1002/grl.50917.

Phan, T. D., J. P. Eastwood, M. A. Shay, J. F. Drake, B. U. Ö. Sonnerup, M. Fujimoto, P. A. Cassak, M. Øieroset, J. L. Burch, R. B. Torbert, A. C. Rager, J. C. Dorelli, D. J. Gershman, C. Pollock, P. S. Pyakurel, C. C. Haggerty, Y. Khotyaintsev, B. Lavraud, Y. Saito, M. Oka, R. E. Ergun, A. Retino, O. L. Contel, M. R. Argall, B. L. Giles, T. E. Moore, F. D. Wilder, R. J. Strangeway, C. T. Russell, P. A. Lindqvist, and W. Magnes (2018), "Electron magnetic reconnection without ion coupling in Earth's turbulent magnetosheath," Nature 557, 202–206, doi: 10.1038/s41586-018-0091-5

Qi, Y., Li, T. C., Russell, C. T., Ergun, R. E., Jia, Y.-D., & Hubbert, M. (2022). Magnetic flux transport identification of active reconnection: MMS observations in earth's magnetosphere. The Astrophysical Journal Letters, 926(2), L34. https://doi.org/10.3847/2041-8213/ac5181

Schwartz, S. J., Thomsen, M. F., Feldman, W. C., and Douglas, F. T. (1987), Electron dynamics and potential jump across slow mode shocks, J. Geophys. Res., 92(A4), 3165– 3174, doi:10.1029/JA092iA04p03165.

Schwartz, S. J., Burgess, D., Wilkinson, W. P., Kessel, R. L., Dunlop, M., & Luehr, H. (1992). Observations of short large-amplitude magnetic structures at a quasi-parallel shock. Journal of Geophysical Research, 97(A4), 4209–4227. https://doi.org/10.1029/91JA02581

Schwartz, S. J., Goodrich, K. A., Wilson, L. B., Turner, D. L., Trattner, K. J., Kucharek, H., et al. (2022). Energy partition at collisionless supercritical quasiperpendicular shocks. Journal of Geophysical Research: Space Physics, 127, e2022JA030637. https://doi.org/10.1029/2022JA030637

Shay, M. A., Haggerty, C. C., Phan, T. D., Drake, J. F., Cassak, P. A., & Wu, P., et al. (2014). Electron heating during magnetic reconnection: A simulation scaling study. Physics of Plasmas, 21(12), 122902. https://doi.org/10.1063/1.4904203

M. A. Shay, C. C. Haggerty, W. H. Matthaeus, T. N. Parashar, M. Wan, and P. Wu (2018), Turbulent heating due to magnetic reconnection, Phys. Plasmas 25, 012304, https://doi.org/10.1063/1.4993423

Stawarz, J. E., Eastwood, J. P., Phan, T. D., Gingell, I. L., Pyakurel, P. S., Shay, M. A., et al. (2022). Turbulence-driven magnetic reconnection and the magnetic correlation length: Observations from Magnetospheric Multiscale in Earth's magnetosheath. Physics of Plasmas, 29(1), 012302. https://doi.org/10.1063/5.0071106

Voros, Z., Yordanova, E., Varsani, A., Genestreti, K. J., Khotyaintsev, Y. V., Li, W.,⋯Saito, Y. (2017). MMS observation of magnetic reconnection in the turbulent magnetosheath. Journal of Geophysical Research: Space Physics, 122, 11,442 – 11,467. https://doi.org/10.1002/2017JA024535

Wang, S., Chen, L.-J., Bessho, N., Hesse, M., Yoo, J., Yamada, M., et al. (2018). Energy conversion and partition in the asymmetric reconnection diffusion region. Journal of Geophysical Research: Space Physics, 123, 8185–8205. https://doi.org/10.1029/2018JA025519

Wang, S., Chen, L.-J., Bessho, N., Hesse, M., Wilson, L. B., Giles, B., et al. (2019). Observational evidence of magnetic reconnection in the terrestrial bow shock transition region. Geophysical Research Letters, 46, 562–570. https://doi.org/10.1029/2018GL080944

Wang, L.-J. Chen, N. Bessho, M. Hesse, L. B. Wilson III, R. Denton, J. Ng, B. Giles, R. Torbert, and J. Burch (2020), " Ion-scale current structures in short largeamplitude magnetic structures," Astrophys. J. 898, 121, doi: 10.3847/1538-4357/ab9b8b

Wilder, F. D., Conley, M., Ergun, R. E., Newman, D. L., Chasapis, A., Ahmadi, N., et al. (2022). Magnetospheric multiscale observations of waves and parallel electric fields in reconnecting current sheets in the turbulent magnetosheath. Journal of Geophysical Research: Space Physics, 127, e2022JA030511. https://doi.org/10.1029/2022JA030511

Wilson, L. B., III (2016), Low frequency waves at and upstream of collisionless shocks, in Low-frequency Waves in Space Plasmas, Geophys. Monogr. Ser., vol. 216, edited by A. Keiling, D.-H. Lee, and V. Nakariakov, pp. 269–291, AGU, Washington, D. C., doi:10.1002/9781119055006.ch16.

Yamada, M., Yoo, J., & Myers, C. E. (2016). Understanding the dynamics and energetics of magnetic reconnection in a laboratory plasma: Review of recent progress on selected fronts. Physics of Plasmas, 23(5), 055402. https://doi.org/10.1063/1.4948721

Zelenyi, L. M.,Malova, H. V., Popov, V. Y., Delcourt, D., Sharma, A. S., and Foss, S. (2004). Nonlinear Equilibrium Structure of Thin Currents Sheets: Influence of Electron Pressure Anisotropy. Nonlin. Process. Geophys. 11, 579–587. doi:10.5194/npg-11-579-2004

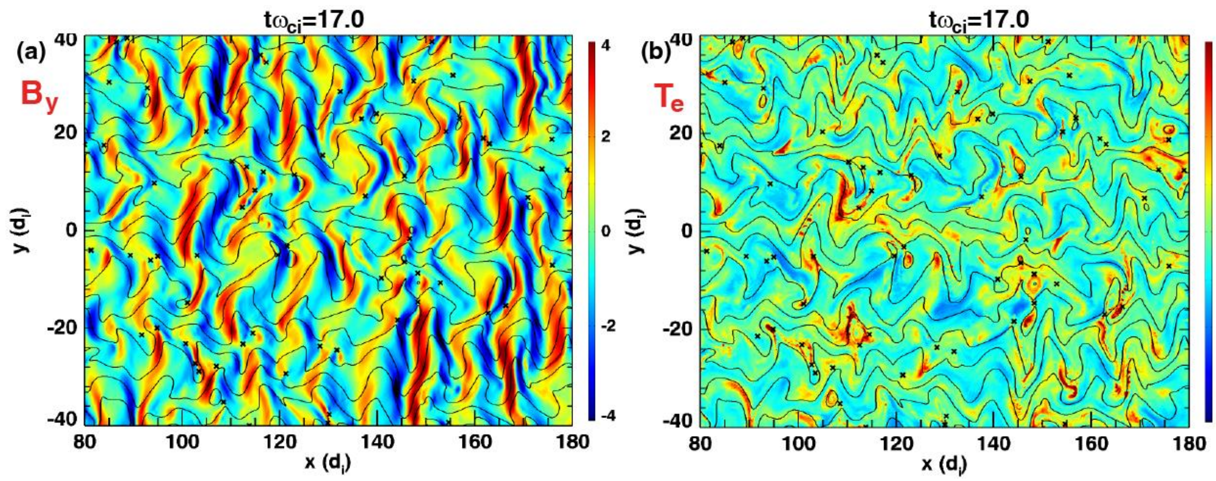

Figure 1. Overview of the simulation. (a) B_y. The vertical stripes are the wave fields from the ion-ion instability, which have been distorted to form current sheets. (b) T_e, which tend to exhibit enhancements in current sheets with sharp bending of field lines (overplotted black curves). The 'X' symbols mark the X-line locations.

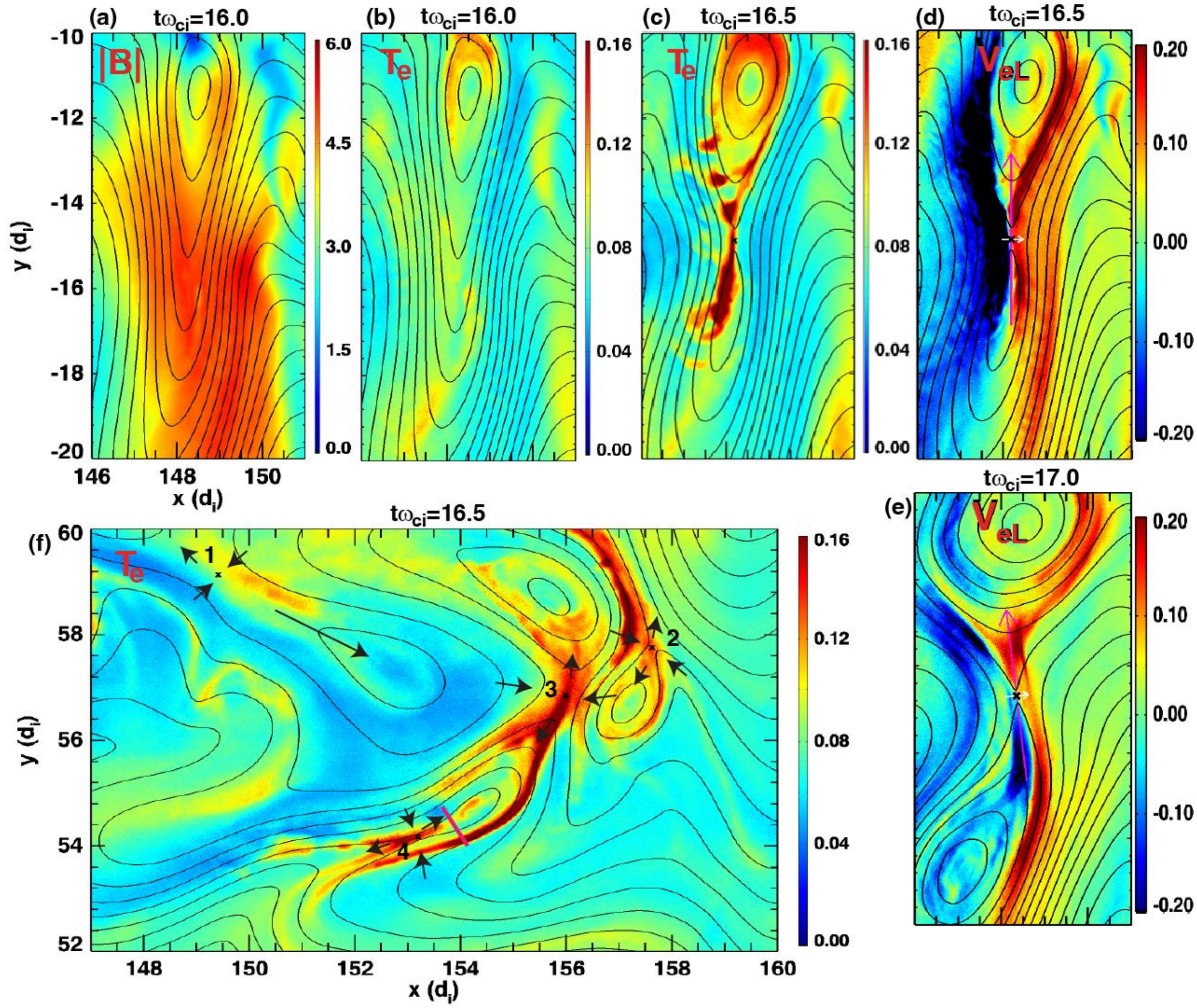

Figure 2. Example reconnection current sheets. (a)-(e) Evolution of an isolated current sheet with the time labelled on top of the panels. (a) Magnetic field amplitude |B|, (b)-(c) T_e showing enhancements in the reconnection current sheet. (d)-(e) Electron velocity along L (V_{eL}) showing a shear flow that evolves into reconnection outflow jets. The magenta and white arrows indicate the L and N directions, respectively. (f) T_e in an example cluster of multiple X-lines. Arrows indicate the inflow and outflow directions of each X-line. It shows the interaction between different reconnection sites.

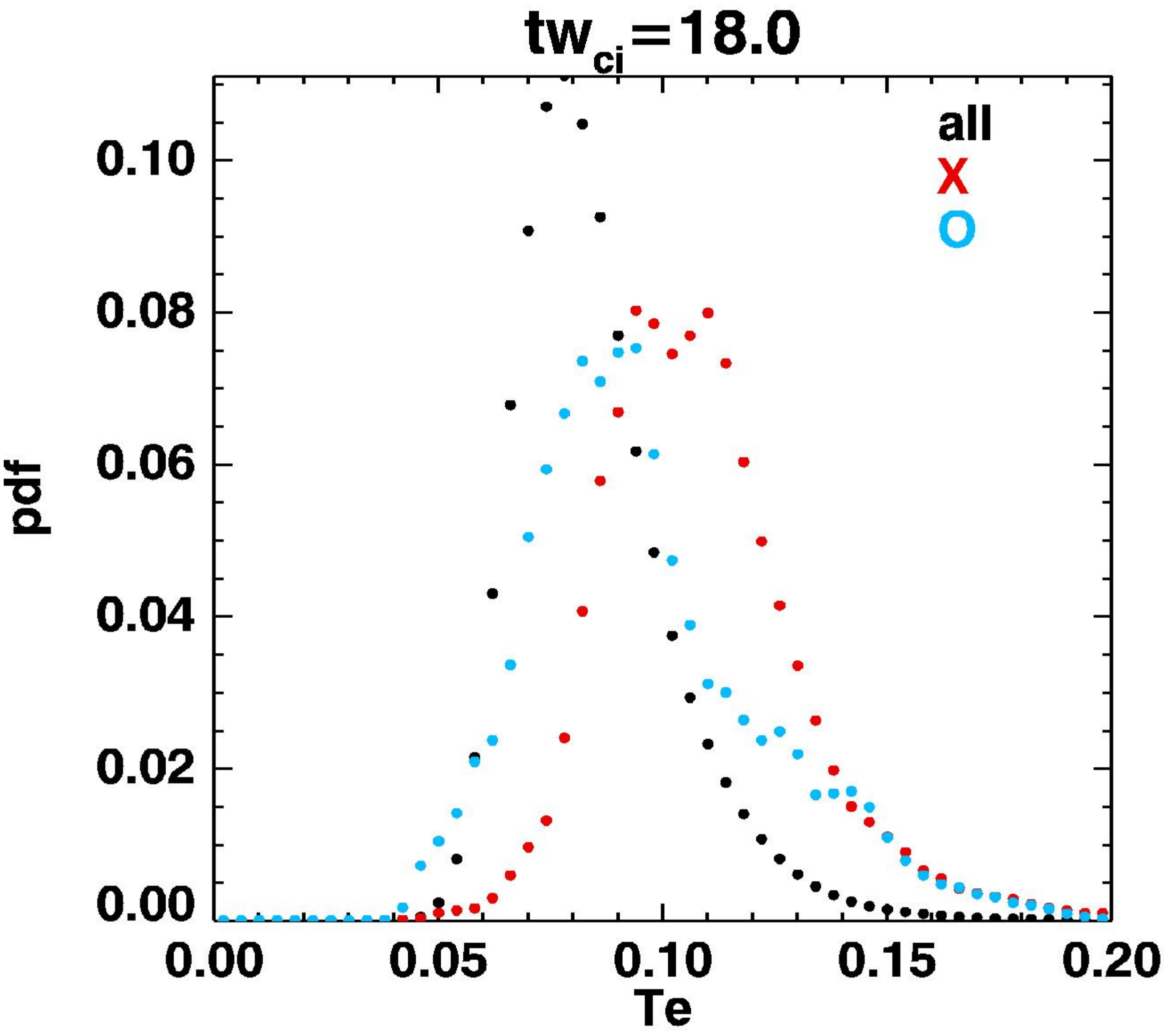

Figure 3. The probability distribution function of T_e at $t\omega_{ci} = 18.0$ with a maximum number of X-lines. Black dots are for all grids in the simulation. Red dots are for grids in 2 d_e × 2 d_e surrounding X-lines, where the distribution shifts to higher T_e. Cyan dots are for grids surrounding O-lines, where the distribution also shifts to higher T_e compared to the black distribution but not as much as the red distribution near X-lines.

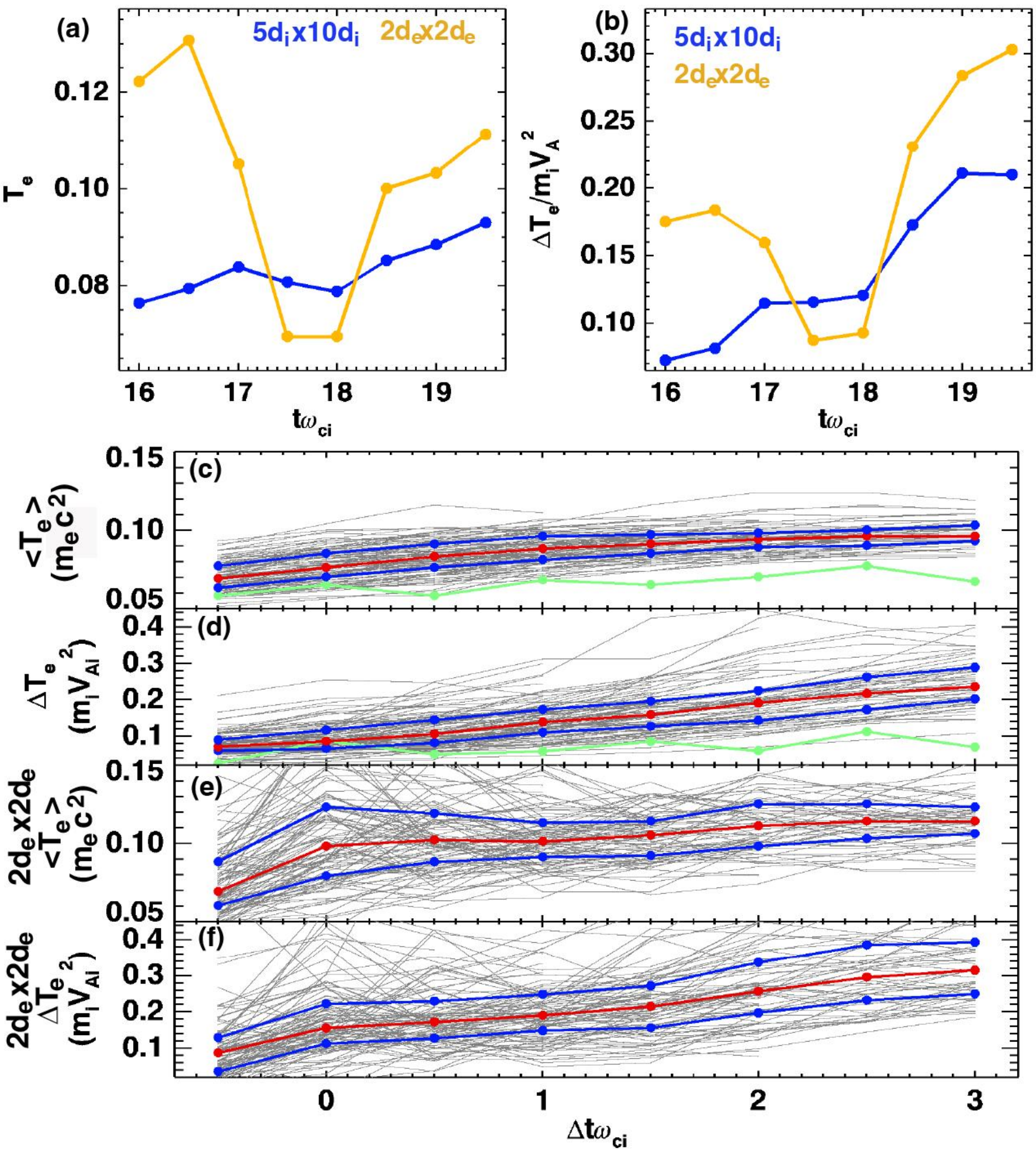

Figure 4. T_e evolution in reconnection current sheets. (a)-(b) T_e evolution over time in the example single current sheet shown in Figure 2 (top). The blue curves represent the average T_e over 5 d_i × 10 d_i that covers the whole current sheet, and orange curves represent the average T_e over 2 d_e × 2 d_e surrounding X-lines. (a) T_e in unit of m_ec^2; (b) heating rate $\Delta T_e/(m_iV_A^2)$, where ΔT_e is the average T_e subtracted by the initial T_e=0.05 m_ec^2, and V_A is based on the average n and |B| over the 5 d_i × 10 d_i region. (c)-(f) Superposed epoch analysis of T_e for 102 events of single or clusters of reconnection current sheets. Epoch t=0 is when the X-line first appears. Gray: curves for individual events; red: median values; blue: 25% and 75% quantiles. (c) average T_e over the d_i-scale region covering the current sheets, and the corresponding heating rate is in (d); (e) average T_e over 2 d_e × 2 d_e surrounding X-lines, and the corresponding heating rate is in (f). The green curve in (c)-(d) are the median values for 17 non-reconnection current sheets. The result shows clear electron heating in reconnection current sheets that increases over time, and the heating rate is 10%~40%.

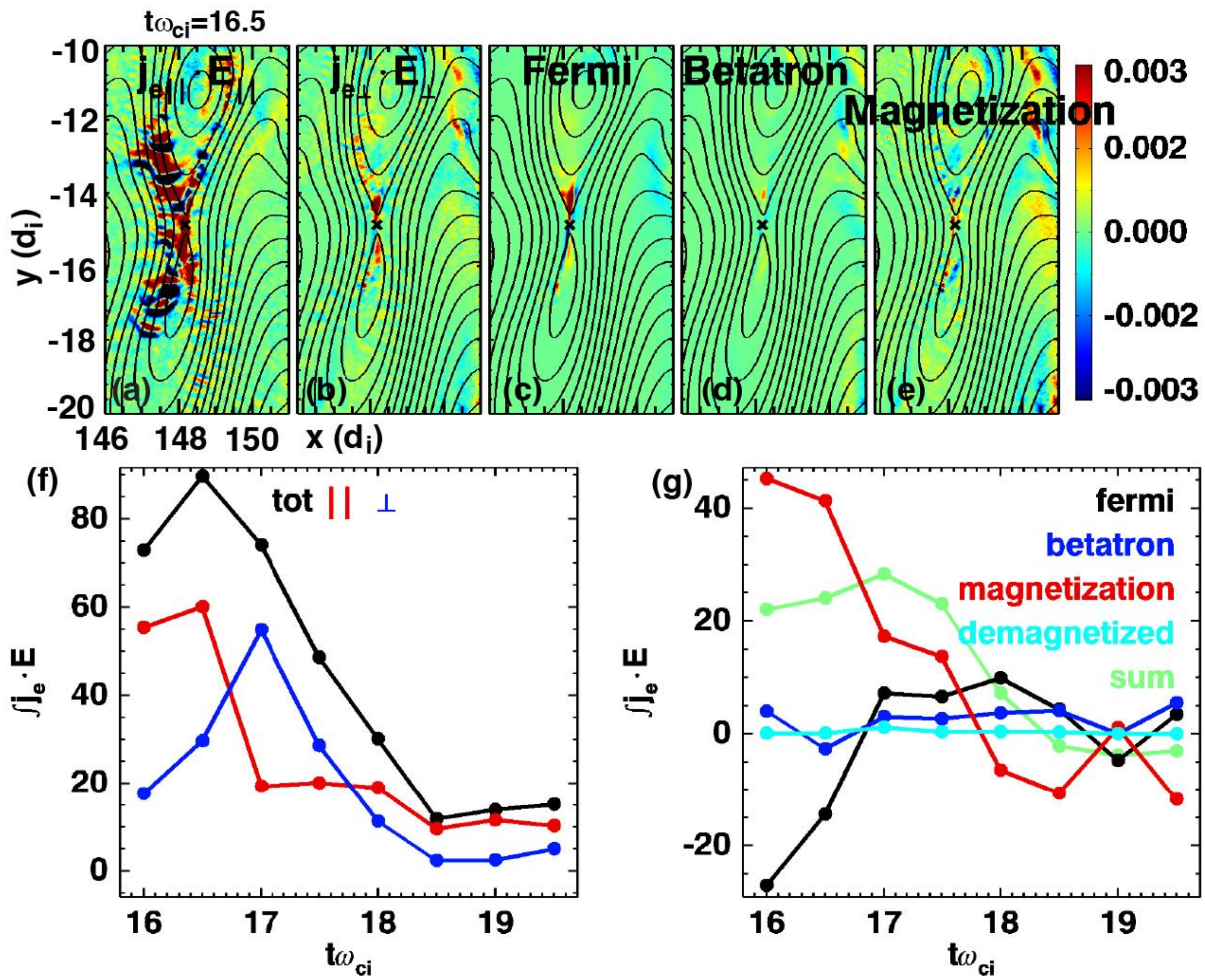

Figure 5. Electron energization represented by $\boldsymbol{j_e} \cdot \boldsymbol{E}$ decomposition for the example single current sheet in Figure 2 (top). (a)-(e) Profiles of decomposed terms at the time when the X-line first appears. (f) The integrated $\boldsymbol{j_e} \cdot \boldsymbol{E}$ over the shown region at different time steps, and the decomposition into the parallel and perpendicular components. (g) Decomposition of $\boldsymbol{j_{e\perp}} \cdot \boldsymbol{E_\perp}$, where 'demagnetized' represents $\boldsymbol{j_{e\perp}} \cdot \boldsymbol{E_\perp}$ in regions with $\mathrm{K} < 1$, and other terms are calculated over regions with $\mathrm{K} > 1$; 'sum' is the summation of the other four terms.

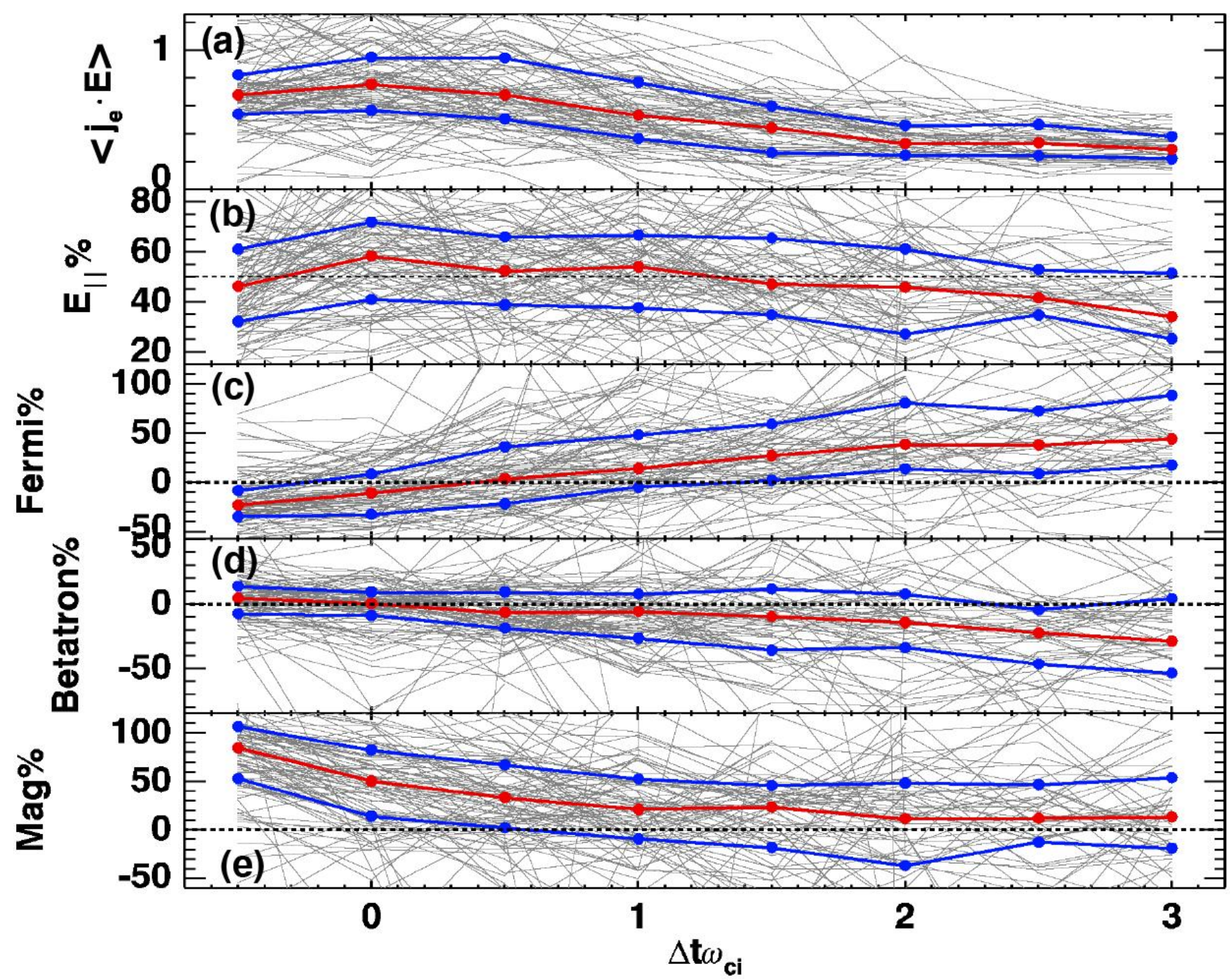

Figure 6. Superposed epoch analysis of $\boldsymbol{j_e} \cdot \boldsymbol{E}$ and its decompositions. The formats are the same with those in Figure 4. (a) Average $\boldsymbol{j_e} \cdot \boldsymbol{E}$ per unit area. (b)-(e) the ratio between each term and total $\boldsymbol{j_e} \cdot \boldsymbol{E}$. At the early time, $E_{\parallel}$ slightly dominates the energization, and the magnetization term dominates the perpendicular energization. The Fermi term exhibits a reversal from negative to positive values and becomes dominant at a couple ω_{ci}^{-1} after reconnection starts.

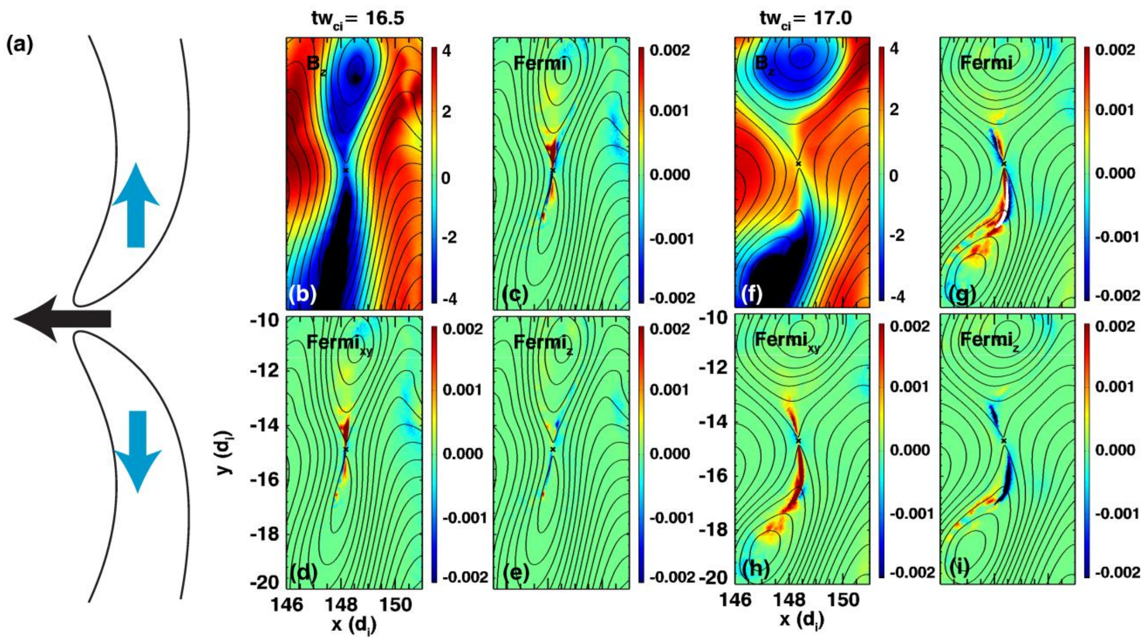

Figure 7. Decomposition of the Fermi term for the example single current sheet. (a) An illustration showing that the flow and curvature are along the same direction for the outflow in the reconnection plane (red), contributing positive Fermi values; the two have opposite signs in the out-of-plane direction due to the Hall effect, which lead to negative values. (b)-(e) are for $t\omega_{ci} = 16.5$ when reconnection starts and the net Fermi contribution is negative. (f)-(i) is for $t\omega_{ci} = 17.0$ with a net positive Fermi contribution. The four panels at each time show B_z, total Fermi term, in-plane Fermi term ($Fermi_{xy}$) and the out-of-plane Fermi term ($Fermi_z$). Overall it shows the competition between the positive in-plane contribution and the negative out-of-plane contribution.

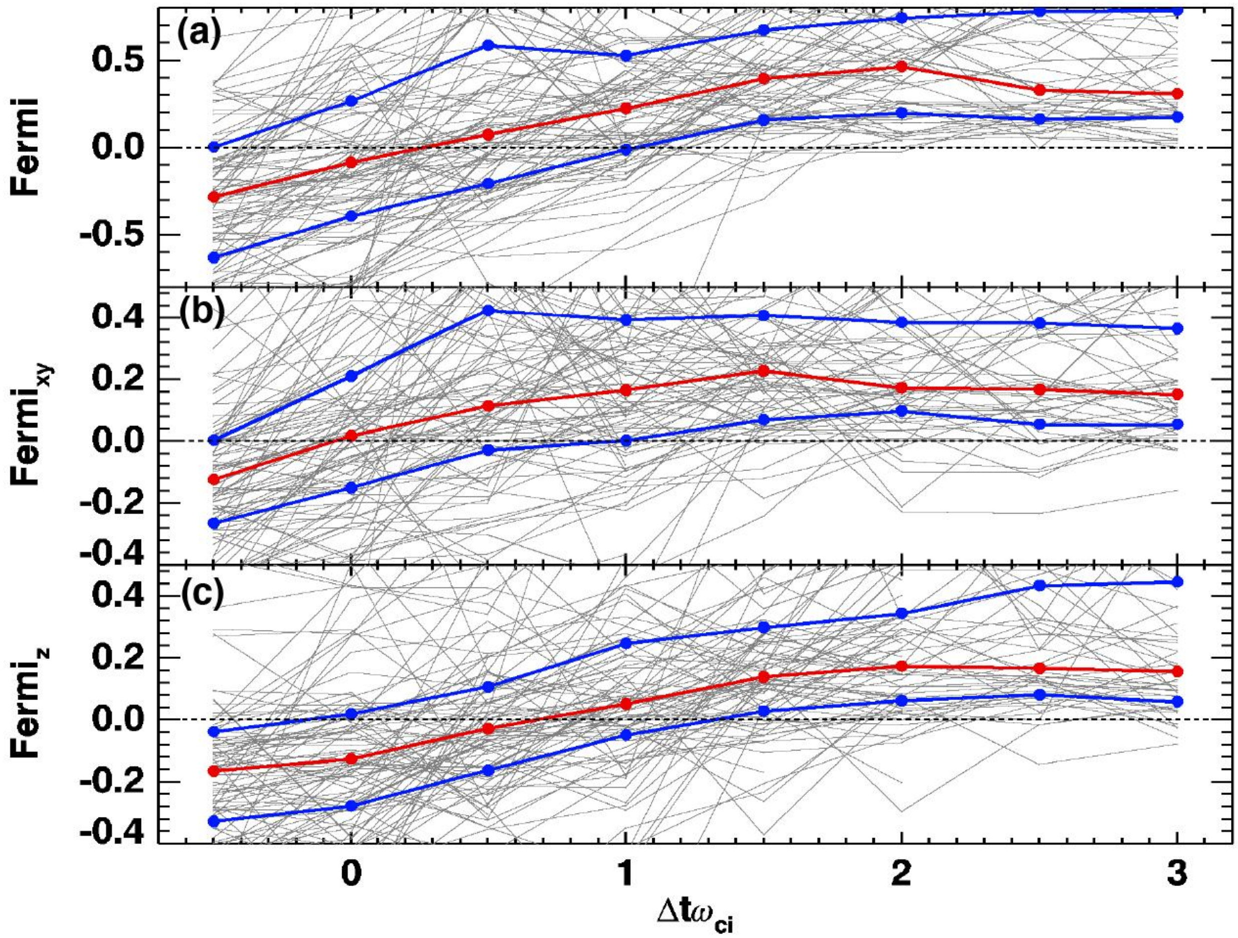

Figure 8. Superposed epoch analysis for Fermi decompositions. The formats are the same with Figure 4. (a) The total Fermi term, (b) in-plane Fermi term (Fermi_{xy}), (c) out-of-plane Fermi term (Fermi_z). Fermi_{xy} is mainly positive, consistent with the reconnection outflow feature, while at the early time before reconnection starts, it can has negative values. Fermi_z stays at negative values for longer time than Fermi_z, associated with the Hall effect, and it can become positive later as the reconnection structure becomes more complicated.

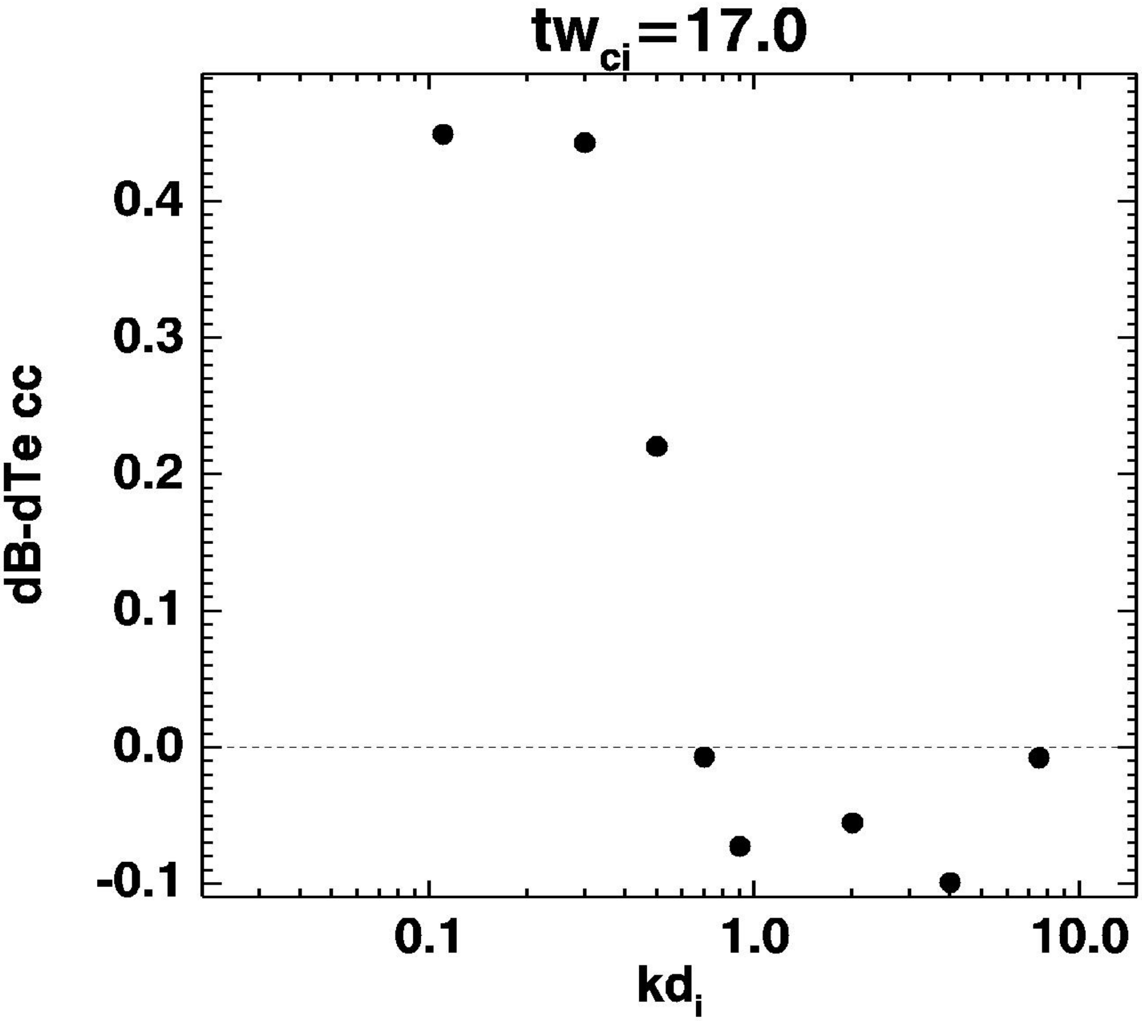

Figure 9. The correlation coefficient between |B| and T_e filtered at different spatial scales. The two quantities exhibit positive correlations at $kd_i \lesssim 0.7$, consistent with the adiabatic heating. Weak negative correlations exist at $kd_i \gtrsim 0.7$, associated with heating contributions by low magnetic field structures like reconnection current sheets.

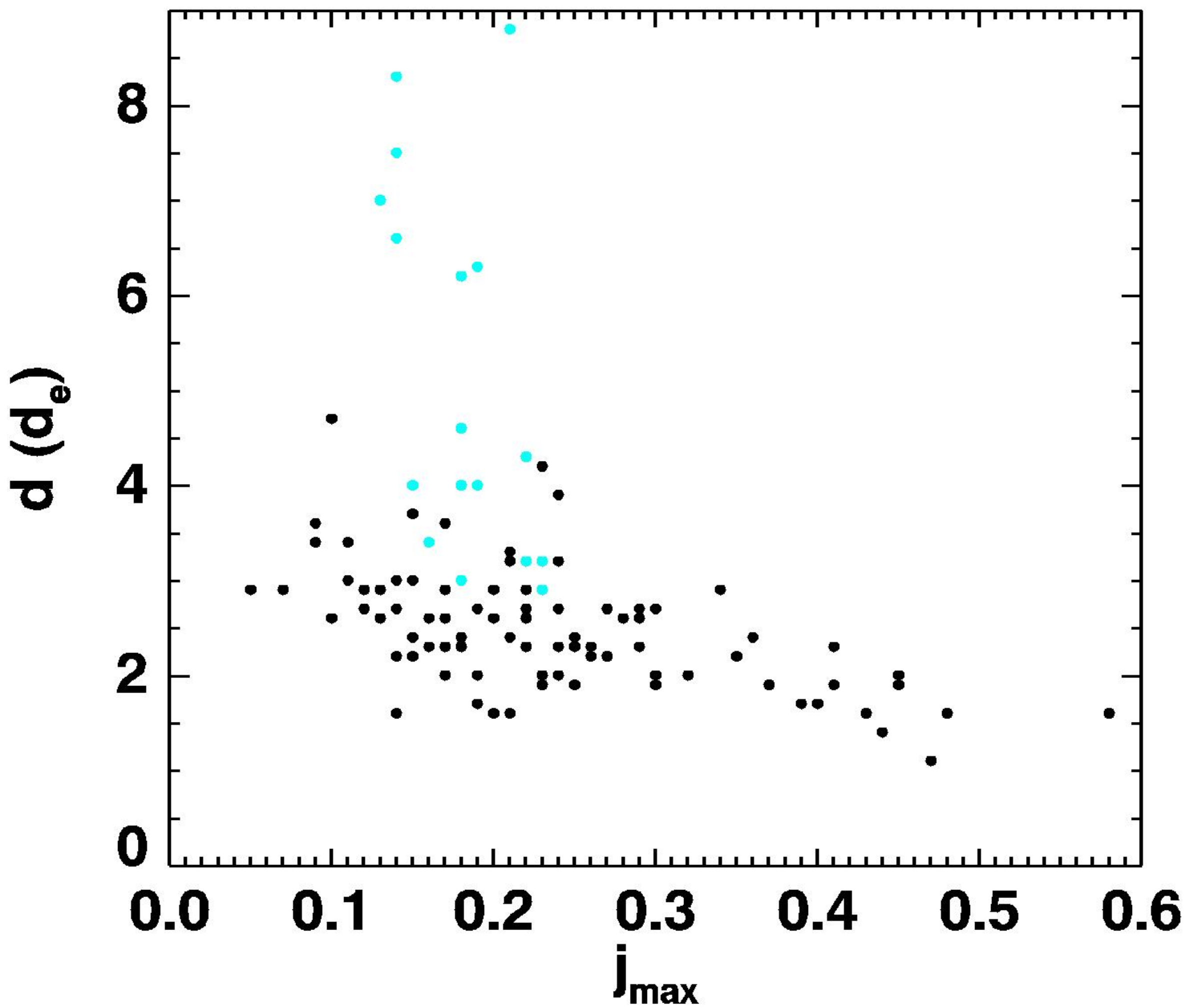

Figure 10. Statistics of the current sheet thickness, represented by the full width at half maximum of $|j_z|$ in a cut along N across the X-line, as a function of the maximum current density. Reconnection current sheets (black) tend to have smaller thicknesses than non-reconnection current sheets (cyan).